



HAL
open science

Soil Thermophysical Properties Near the InSight Lander Derived From 50 Sols of Radiometer Measurements

Sylvain Piqueux, Nils Müller, Matthias Grott, Matthew Siegler, Ehouarn Millour, Francois Forget, Mark Lemmon, Matthew Golombek, Nathan Williams, John Grant, et al.

► **To cite this version:**

Sylvain Piqueux, Nils Müller, Matthias Grott, Matthew Siegler, Ehouarn Millour, et al.. Soil Thermophysical Properties Near the InSight Lander Derived From 50 Sols of Radiometer Measurements. *Journal of Geophysical Research. Planets*, 2021, 126 (8), 10.1029/2021JE006859 . hal-03457076

HAL Id: hal-03457076

<https://hal.science/hal-03457076>

Submitted on 9 Dec 2021

HAL is a multi-disciplinary open access archive for the deposit and dissemination of scientific research documents, whether they are published or not. The documents may come from teaching and research institutions in France or abroad, or from public or private research centers.

L'archive ouverte pluridisciplinaire **HAL**, est destinée au dépôt et à la diffusion de documents scientifiques de niveau recherche, publiés ou non, émanant des établissements d'enseignement et de recherche français ou étrangers, des laboratoires publics ou privés.


















Distributed under a Creative Commons Attribution - NonCommercial - ShareAlike 4.0 International License

Soil Thermophysical Properties Near the InSight Lander Derived From 50 Sols of Radiometer Measurements

**Key Points:**

- The InSight radiometers measured surface temperatures multiple times per sol over a flat and homogeneous patch of Martian soil
- The thermal inertia of the soil in Homestead hollow is $\sim 183 \pm 25 \text{ J m}^{-2} \text{ K}^{-1} \text{ s}^{-1/2}$, consistent with aeolian fine sand infilling
- The presence of a duricrust suggested by imagery is difficult to reconcile with this thermal inertia value

Sylvain Piqueux¹ , Nils Müller² , Matthias Grott² , Matthew Siegler³ , Ehouarn Millour⁴ , Francois Forget⁴, Mark Lemmon⁵ , Matthew Golombek¹ , Nathan Williams¹ , John Grant⁶ , Nicholas Warner⁷ , Veronique Ansan⁸, Ingrid Daubar⁹ , Jörg Knollenberg², Justin Maki¹ , Aymeric Spiga⁴ , Don Banfield¹⁰, Tilman Spohn^{2,11} , Susan Smrekar¹, and Bruce Banerdt¹ 

¹Jet Propulsion Laboratory, California Institute of Technology, Pasadena, CA, USA, ²DLR Institute for Planetary Research, Berlin, Germany, ³Southern Methodist University, Dallas, TX, USA, ⁴Sorbonne Université, Paris, France, ⁵Space Science Institute, College Station, TX, USA, ⁶National Air and Space Museum, Smithsonian Institution, Washington, DC, USA, ⁷State University of New York at Geneseo, Geneseo, NY, USA, ⁸Université de Nantes, Nantes, France, ⁹Brown University, Providence, RI, USA, ¹⁰Cornell University, Ithaca, NY, USA, ¹¹International Space Science Institute ISSI, Bern, Switzerland

Correspondence to:

S. Piqueux,
sylvain.piqueux@jpl.caltech.edu

Citation:

Piqueux, S., Müller, N., Grott, M., Siegler, M., Millour, E., Forget, F., et al. (2021). Soil thermophysical properties near the InSight lander derived from 50 sols of radiometer measurements. *Journal of Geophysical Research: Planets*, 126, e2021JE006859. <https://doi.org/10.1029/2021JE006859>

Received 21 FEB 2021
 Accepted 19 APR 2021

Abstract Measurements from the InSight lander radiometer acquired after landing are used to characterize the thermophysical properties of the Martian soil in Homestead hollow. This data set is unique as it stems from a high measurement cadence fixed platform studying a simple well-characterized surface, and it benefits from the environmental characterization provided by other instruments. We focus on observations acquired before the arrival of a regional dust storm (near Sol 50), on the furthest observed patch of soil (i.e., ~ 3.5 m away from the edge of the lander deck) where temperatures are least impacted by the presence of the lander and where the soil has been least disrupted during landing. Diurnal temperature cycles are fit using a homogenous soil configuration with a thermal inertia of $183 \pm 25 \text{ J m}^{-2} \text{ K}^{-1} \text{ s}^{-1/2}$ and an albedo of 0.16, corresponding to very fine to fine sand with the vast majority of particles smaller than $140 \mu\text{m}$. A pre-landing assessment leveraging orbital thermal infrared data is consistent with these results, but our analysis of the full diurnal temperature cycle acquired from the ground further indicates that near surface layers with different thermophysical properties must be thin (i.e., typically within the top few mm) and deep layering with different thermophysical properties must be at least below ~ 4 cm. The low thermal inertia value indicates limited soil cementation within the upper one or two skin depths (i.e., ~ 4 –8 cm and more), with cement volumes $\ll 1\%$, which is challenging to reconcile with visible images of overhangs in pits.

Plain Language Summary InSight carried a six-channel radiometer used to measure diurnal surface temperatures over the duration of the mission. Surface temperatures are controlled by insolation and the microscopic physical properties of the soil (typical grain size, density, degree of soil cementation, or internal layering) that could not be resolved without a microscope or other instruments. Because the InSight lander does not have any systematic way to interrogate the soil, we have instead analyzed these temperature data and characterized the near-surface soil properties. We found that the soil structure near the lander is homogeneous within the top few cm, and is made of loose sandy material with very little to no cementation. These properties are consistent with those derived from orbit before landing using remote sensing techniques, but difficult to reconcile with visible imagery showing evidence for induration farther from the hollow margin.

1. Introduction

The Interior Exploration using Seismic Investigations, Geodesy and Heat Transport mission (InSight; Banerdt et al., 2020) landed on Mars in Elysium Planitia, on November 26, 2018, with the goal of understanding the formation and evolution of terrestrial planets through the investigation of the interior structure of Mars. To meet these objectives, the lander carries multiple instruments, including the Heat Flow and Physical Properties Package (HP³; Spohn et al., 2018) that consisted of a penetrator, colloquially referred to as “the mole,” a tether equipped with platinum resistance temperature sensors (TEM-P), and a suite of

© 2021. Jet Propulsion Laboratory, California Institute of Technology. Government sponsorship acknowledged.

This is an open access article under the terms of the [Creative Commons Attribution-NonCommercial License](https://creativecommons.org/licenses/by-nc/4.0/), which permits use, distribution and reproduction in any medium, provided the original work is properly cited and is not used for commercial purposes.

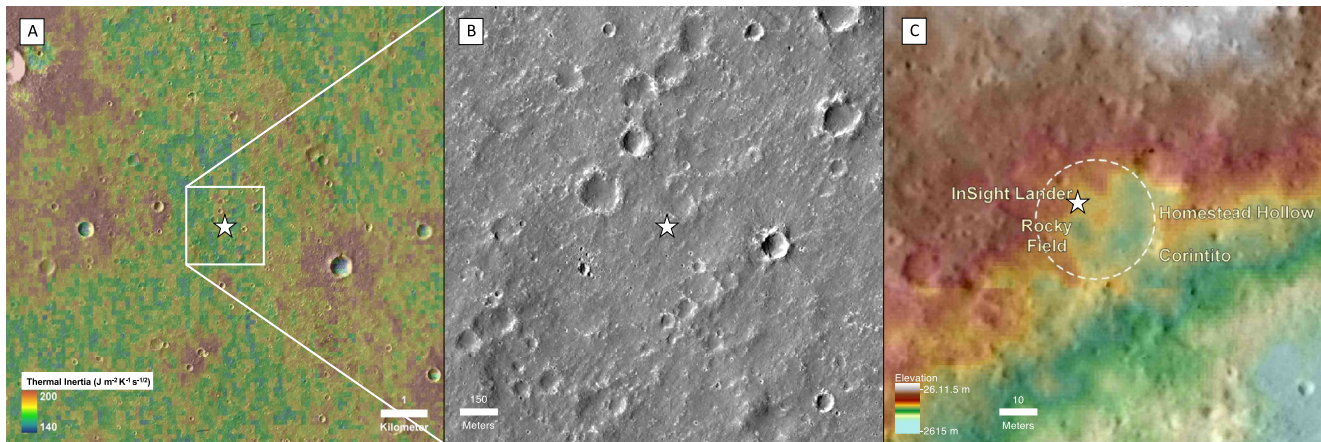


Figure 1. (a) THEMIS-derived regional thermal inertia map centered on the InSight landing site (star, 4.5°N, 135.6°E) overlain on a CTX mosaic, modified from Golombek et al. (2017). (b) HiRISE image ESP_036761_1845, the star indicates the position of the lander. (c) Topographic map of Homestead hollow (modified from Golombek, Warner, et al., 2020, see their Figure S5 for details). Dashed circle is Homestead hollow, Rocky field is a rougher and rockier section in the western portion of the hollow, and Corintito is a nearby Corinto secondary crater.

radiometers (RAD) positioned underneath the deck. The RAD determined surface temperatures through radiance measurements at three distinct wavelengths windows, and at two locations northwest of the lander. The data set generated by the RAD (InSight_RAD_Science_Team, 2019) is exceptional: unlike previous temperature sensing assets deployed at the surface of Mars used for thermophysical characterizations (Edwards et al., 2018; Fergason et al., 2006; Spanovich et al., 2006; Vasavada et al., 2017; Zent et al., 2010), this fixed platform repeatedly measures unobstructed ground temperatures of a homogeneous and well-characterized patch of soil, while other instruments (i.e., weather package and cameras Banfield et al., 2019; Maki et al., 2018) provide information of the surrounding environment.

Further, a significant team effort has led to a thorough characterization of the landing region before arrival at Mars as part of the landing site selection and certification effort, but also after touching down to assess the physical and geological properties of the surrounding area (Golombek, Kass, et al., 2020; Golombek et al., 2017, 2018; Golombek, Warner, et al., 2020; Golombek, Williams, et al., 2020). In short, InSight landed in western Elysium Planitia (4.5°N, 135.6°E) at a MOLA (Zuber et al., 1992) elevation of -2.6 km on smooth volcanic Hesperian to Early Amazonian plains, where rock abundance is generally low (i.e., ~ 1 – 2%), and where steep slopes (i.e., $>15^\circ$) are uncommon (Golombek et al., 2017; Grant et al., 2020; Warner et al., 2020; Weitz et al., 2020). TES (Christensen et al., 2001) and THEMIS (Christensen et al., 2004) temperature data are consistent with typical regional thermal inertia of 140 – 200 $\text{J m}^{-2} \text{K}^{-1} \text{s}^{-1/2}$ (230 and 166 $\text{J m}^{-2} \text{K}^{-1} \text{s}^{-1/2}$ at the lander location, respectively) interpreted as cohesionless fine sand, without significant thermally thick dust mantling (Figure 1) (Golombek, Kass, et al., 2020; Golombek et al., 2017). The absence of unambiguous seasonal variations in apparent thermal inertia from orbital data was interpreted as an indication of the absence of steep thermal inertia changes that would have been caused by underlying bedrock or water ice within the top few tens of cm of the surface (Golombek, Warner, et al., 2020). After landing, the analysis of the images of material excavated from pits produced by the retro-rockets and the mole, show that the lander settled in a smooth sandy, pebble-rich circular depression (*Homestead hollow*, Figure 1c) interpreted as a highly degraded ~ 27 m diameter impact crater (Golombek, Warner, et al., 2020; Golombek, Williams, et al., 2020; Grant et al., 2020; Warner et al., 2020) surrounded by rockier and rougher terrain. The crater depression has been filled with fine windblown sand-size material, intermixed with numbers of cm-size pebbles and rocks.

Below a thin layer of unconsolidated soil at Homestead hollow, stronger layers show some cohesion, though the degree to which it is cemented remains uncertain, with important implications both for the penetrability of the soil by the HP³ mole (Spohn et al., 2018) and for our understanding of the Martian soil formation and evolution (Warner et al., 2017, 2020). Whether these lightly cemented horizons extend to or beyond the hollow interior, however, is a subject of debate. Every landing site on Mars, numerous roving locations, and general considerations using orbital data confirm that soil encrustations, generally referred to as duricrust,

are common throughout the planet (Arvidson, Anderson, Bartlett, Bell, Balney, et al., 2004; Arvidson, Anderson, Bartlett, Bell, Christensen, et al., 2004; Arvidson et al., 1989, 2006; Binder et al., 1977; Herkenhoff et al., 2008; Jakosky & Christensen, 1986; Mellon et al., 2009; Moore et al., 1999; Mutch et al., 1977; Shaw et al., 2009). These materials are consistent with observations of coherent platy soil clasts near the lander, as well as steep walled exposures in pits showing small rocks and pebbles in a finer-grained matrix (Golombek, Warner, et al., 2020).

In previous efforts, multiple teams have analyzed surface temperature data acquired from the ground to characterize the Martian surface layer:

1. Using the Miniature Thermal Emission Spectrometer (Christensen et al., 2003) onboard the Mars Exploration Rovers, Fergason et al. (2006) performed both the first ground-based derivation of thermal inertia, and a comparison with orbital values (Golombek et al., 2008). Using microscope imagery (Herkenhoff et al., 2003) and synchronous atmospheric characterization (Smith et al., 2006), they confirmed that fines, rocks, desert pavements, and bedforms are associated with the expected thermal inertia values, and they validated relationships between grain sizes and thermal properties established in the laboratory (Presley & Christensen, 1997).
2. Hamilton et al. (2014), Martinez et al. (2014), and Vasavada et al. (2017) modeled seasonal and diurnal temperature curves derived from the Ground Temperature Sensor (GTS) on Curiosity's Rover Environmental Monitoring Station (REMS; Sebastian et al., 2010) at Gale crater over a wide range of surface materials, and found distinct thermal behavior between fines, mudstones and sandstones. Their work demonstrated the value of recording the full diurnal temperature cycle for the deconvolution of vertical and horizontal heterogeneities.
3. A similar approach was adopted by Edwards et al. (2018), but focused more specifically on well-sorted aeolian material (Bagnold dunes in Gale crater) for which microscopic imagery was available (Edgett et al., 2012). They concluded that for well-sorted material, thermally derived grain sizes reliably match those resolved in situ in images. Coarse (armor-like) or slightly indurated material does not impact the amplitude or shape of the temperature curves as long as that top layer is <5 mm in thickness (in the case of sand size material).

In this study, we contribute to this ongoing Martian soil characterization effort by leveraging the uniqueness of the InSight RAD measurements (i.e., repeated full diurnal cycle acquisitions, fairly simple and well-characterized soil surface, availability of environmental characterization including atmospheric pressure and dust opacity τ). We solely focus on the first 50 sols of the mission to avoid: (a) possible seasonal cycles of dust removal and redeposition (Newman & Richardson, 2015; Szwast et al., 2006; Vicente-Retortillo et al., 2018); (b) seasonal atmospheric trends such as radiatively active clouds that impact surface temperatures near the equator (Wilson & Guzewich, 2014; Wilson et al., 2008); (c) heat contribution from deeper layering that would manifest itself over seasonal times scales (Edwards et al., 2011; Piqueux et al., 2019; Putzig & Mellon, 2007a); (d) and the complicating effect of the regional dust storm (Plesa et al., 2016; Streeter et al., 2019) that occurred near Sol 50 (Banfield et al., 2020). Our results complement other analysis efforts focused on measurements acquired during/after several Phobos transits (i.e., focusing on the top few 100's of μm to mm of the surface layer; Mueller et al., 2021; Mueller, Grott, et al., 2020), on long term seasonal trends probing deeper into the subsurface, and in situ thermal conductivity/diffusivity measurements (Grott, Spohn, Knollenberg, Krause, Hudson, et al., 2021; Grott, Spohn, Knollenberg, Krause, Nagihara, et al., 2021).

2. Approach

2.1. RAD Data Set

RAD is composed of two pairs of three thermopile sensors (i.e., radiometers) mounted under the deck of the lander, and observes the surface to the north-northwest of the lander, which is opposite to where the SEIS and HP³ instruments have been deployed, at an azimuth of $\sim 340^\circ$ (measured clockwise from north, Figure 2). One of the sensor suite (“near RAD”) observes the soil closest to the lander (boresight at $\sim 55^\circ$ from the horizon, i.e., \sim half a meter away from the closest edge of the deck), and the “far RAD” observes the surface ~ 3.5 m away from the closest edge of the deck. At these distances, the lander blocks approximately half and 4% of the sky, respectively, and the resulting surface emission angle is $\sim 35^\circ$ and $\sim 65^\circ$ for

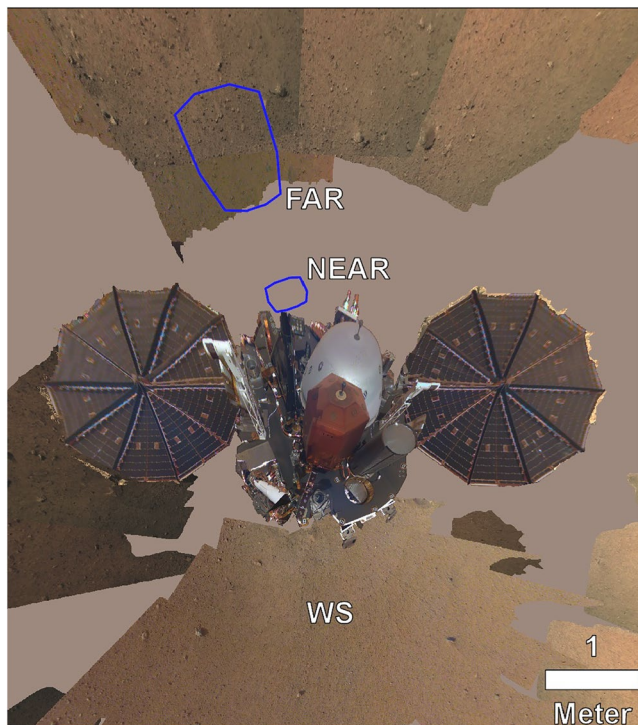


Figure 2. Position of the far (FAR) and near (NEAR) radiometers (RAD) spots relative to the lander, together with the workspace (WS) where instruments have been deployed (Golombek, Williams, et al., 2020). North is up. Sol 10 image D_LRGB_0010_CPG 040010RR_S_RAD_5MMM1 of the far rad spot, sol 10 deck mosaic (tie-pointed for approximate location and scale, but not orthorectified, explaining internal distortions), sol 14 workspace mosaic, and orthomosaic D_LRGBI0160XILT030100ORRAS_5MM_35MM1 encompassing several sols of image data. Approximate resolution of 5 mm/pixel near the lander.

the near and far RAD spot, respectively. In this study, we only discuss data acquired at the far RAD location because unlike the near RAD spot, it does not experience complex transient shadows cast by the solar panels, and it is least impacted by the radiative and reflective presence of the lander. In addition, due to hardware design constraints, the far radiometer spot has received the best imaging and characterization of the two RAD spots. Further, the far RAD location presents the least disrupted soil caused by the retro-rockets during landing (Golombek, Kass, et al., 2020; Golombek, Warner, et al., 2020).

The three radiometers of each of the near and far RAD sensors are centered at 8–14, 7.8–9.6, and 16–19 μm . Calibration procedures and measurements error/uncertainties are described in Mueller, Knollenberg, et al. (2020), systematically provided as part of the data delivery, and depicted in this study as error bars associated with each measurement (or binned measurements). In this study, we only use the 8–14 μm channel because the atmosphere is largely transparent at these wavelengths, and peak thermal infrared emission oscillates between 10 and 15 μm over a typical Sol (Wien's law), thus providing the best signal for this analysis. Temperature data are acquired by 24 sets of 23 measurements over 5-min periods, yielding excellent diurnal temperature curve sampling with hourly resolution, starting on Sol 16. In addition, data generation and return are driven by numerous other factors including science activity prioritization, and availability of onboard or Deep Space Network resources.

2.2. Surface Properties From Imagery

As part of the SEIS and HP³ instrument placement, imagery was acquired to provide a thorough characterization of the patch of soil observed by the far RAD (Figure 3). The far RAD spot measures $\sim 0.9 \times \sim 1.4$ m, centered ~ 4.5 m away from the center of the lander, on terrain locally dipping $\sim 4^\circ$ toward the east-southeast (100° azimuth) at the scale length of the RAD footprint, steeper than the regional slope (i.e., $<1^\circ$ slope at the scale length of hundreds of meters toward the east). It is located within,

but near the edge of Homestead hollow (Figure 1) on a unit displaying similar properties as those observed elsewhere within the crater: smooth, filled primarily with aeolian sand, some surface dust, as well as granules and pebbles (1–7 mm).

Golombek, Warner, et al. (2020) provide a description of the clasts observed within the radiometer footprint: these authors were able to identify 41 individual rocks 5 cm–5 mm in size over an area of 1.08 m², with a reported measurement uncertainty of 2–4 mm. The cumulative fraction area of rocks 3 cm or larger approaches 2% (Golombek, Kass, et al., 2020; Golombek, Warner, et al., 2020). Clasts this small (i.e., $<<15$ cm, the size of a diurnal skin depth in bedrock; Christensen, 1986; Nowicki & Christensen, 2007) and with such modest occurrence have no appreciable effect on the thermal inertia (Golombek et al., 2003), and are ignored in the rest of this work. As a result, the radiometer spot is treated as laterally homogeneous.

The far RAD spot is located well within the area near the lander darkened by a factor $\sim 35\%$ (relative albedo) when compared to the surrounding terrains, as a result of the surficial dust removal caused by the retrorockets during the landing (Golombek, Warner, et al., 2020). Under the lander and by the mole located on the opposite side of the spacecraft in the Workspace (i.e., “WS” in Figure 2), two pits expose subsurface material interpreted as poorly sorted with pebble/cobble size clasts. Generally, the stratigraphy of the top few cm near the lander as illustrated in Figure 4 and imagery near and under the lander consists of (a) some dust a few microns thick at most, (b) ~ 1 cm of unconsolidated material, on (c) an apparently more cohesive unit of variable thickness, that is, underlain with (d) unconsolidated sand and intermixed small pebbles and rocks. Although increased cohesion can be observed in polydisperse mixtures and non-ideal grains compared to homogenous samples made of spherical grains (Pohlman et al., 2006; Statham, 1974), overhanging

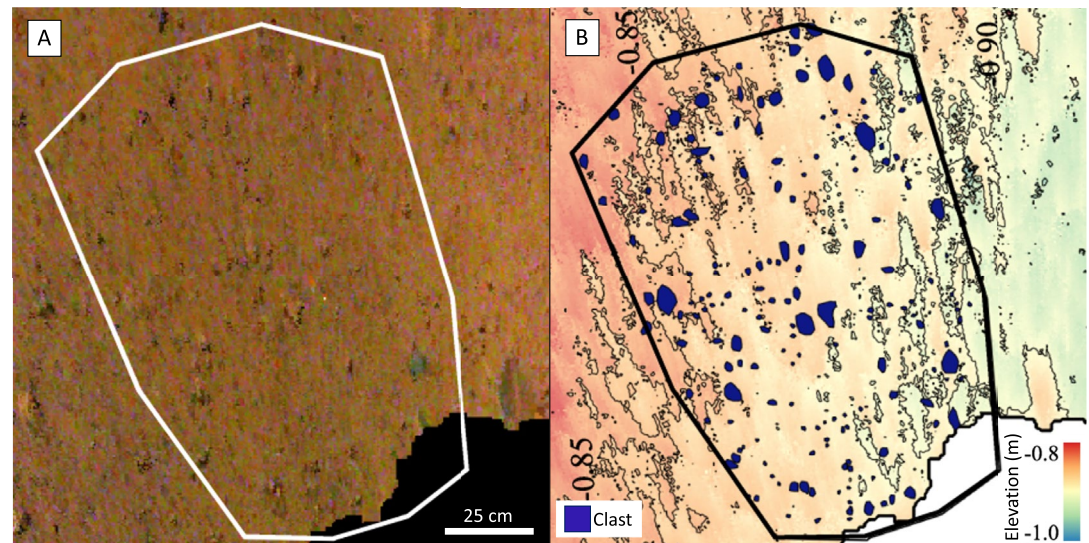


Figure 3. (a) Projected Instrument Deployment Camera (IDC) image (D_LRGB_0010_CPG040010ORR_S_RAD_5MMM1) in equi-rectangular projection centered on lander deck robotic arm, with a spatial resolution of 5 mm per pixel. North is up. White box shows the surface covered by the radiometer monitoring. (b) Elevation model on the same area acquired by stereo IDC images. The elevation corresponds to the vertical height relative to the lander deck, negative downwards with an accuracy of 1 cm. The interval of contour lines (black line) is 5 cm, showing that the surface is slightly tilted toward ESE. The clast, greater than 1 cm, are mapped in blue within the radiometer area.

layers in the mole pit (Figure 4) and relatively high cohesion values derived from arm/scoop experiments (Marteau et al., 2021) argue for the presence of a cementing phase, that is, for the existence of a duricrust similar to those observed at most landing and roving locations on Mars (Arvidson et al., 1989, 2006; Binder et al., 1977; Golombek et al., 2008; Herkenhoff et al., 2008; Minitti et al., 2013; Moore et al., 1999; Mutch et al., 1977; Shaw et al., 2009; Sullivan et al., 2011; Wang et al., 2006; Weitz et al., 2006). Only fine sand and

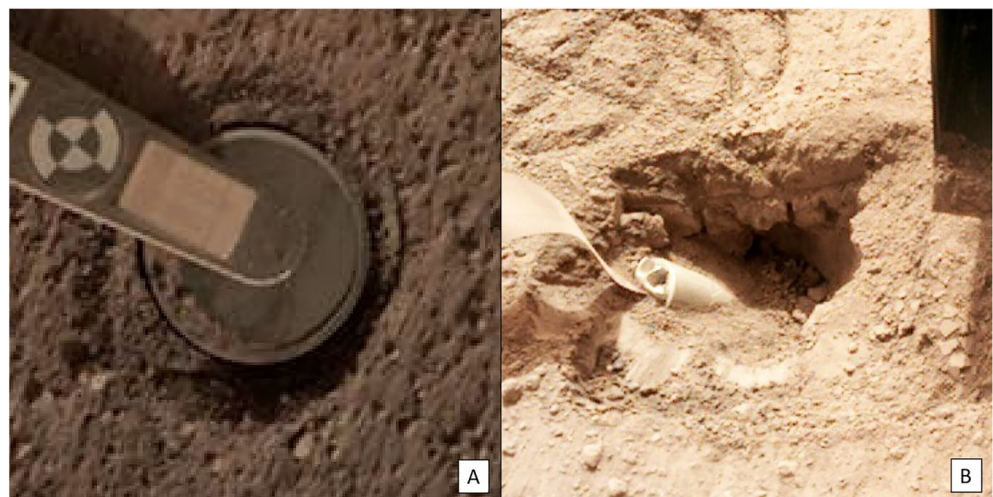


Figure 4. (a) Subset of image D000M0118_607019065EDR_F0000_0250M4 showing one of the circular feet (80 mm across) of the HP³ support structure displaced after a series of mole hammering attempt. This image suggests a loose top layer at least ~1 cm in thickness. (b) Subset of image D000M0577_647739954EDR_F0000_0930M showing the partially buried mole (2.7 cm diameter) in its pit (on the left). The steep walls in the mole pit and overhang are indicative of a cohesive soil and suggestive of cementation over a thickness at least comparable to a diurnal skin depth (i.e., ~4 cm). Imagery under the lander further indicates that the cohesive layer is at least 10 cm in thickness (Golombek, Warner, et al., 2020). The overhang is a strong indicator for the presence of a duricrust.

Table 1
Soil and Atmosphere Parameters Used for the Modeling

| Quantity | Value | Unit | Reference |
|--|-----------|--------|---|
| Slope | 4 | degree | Figure 3 |
| Slope Azimuth | 100 | degree | Figure 3 |
| Emissivity | 0.98 | | Hamilton et al. (2014) |
| Dust Opacity | 0.79–1.90 | | Banfield et al. (2020) |
| Latitude | 4.5 | degree | Golombek, Warner, et al. (2020); Golombek, Williams, et al. (2020) |
| Longitude | 135.6 | degree | Golombek, Warner, et al. (2020); Golombek, Williams, et al. (2020) |
| Elevation | −2613 | meter | Golombek, Warner, et al. (2020); Golombek, Williams, et al. (2020) |
| Dust Single Scattering Albedo | 0.94 | | Vasavada et al. (2017) |
| Dust Visible/IR extinction coefficient | 0.41 | | Vasavada et al. (2017) |
| Henry-Greenstein asymmetry factor | 0.6 | | Vasavada et al. (2017) |

no to very weak induration stemming from cementation was expected based on a pre-landing assessment (Golombek et al., 2017).

2.3. Numerical Model and Approach

2.3.1. Numerical Model and Fitting Procedure

The soil thermophysical properties are constrained using surface temperatures measured at the far RAD location. All temperature fits presented in this study are performed using the KRC thermal model version 3.6.5. The numerical code is extensively described in Kieffer (2013), as well as in other study focused on ground-based (Edwards et al., 2018; Fergason et al., 2006; Hamilton et al., 2014; Vasavada et al., 2017), or orbital (Edwards & Piqueux, 2016; Piqueux et al., 2019) observations. Table 1 provides selected input parameters used to perform the analysis described in this study. Thermal conductivity dependence on temperature is taken from Morgan et al. (2018) (see references therein), and specific heat capacity is taken from Vu et al. (2019) assuming a Martian meteorite basaltic composition. The thermal inertia and thermometric albedo derivations procedures follow the steps described next and are summarized in Figure 5. All brightness temperatures are corrected for non-unit emissivity assuming a broadband emissivity $\epsilon = 0.98$, a typical value for fine Martian soil (Hamilton et al., 2014). These authors also show that potential errors resulting from emissivity uncertainties are certainly ≤ 2 K, and mostly impact the derivation of radiometric albedos, and much less so the absolute thermal inertia values because the amplitude of the diurnal temperature curves remains largely unaffected by emissivity errors. All derivations are performed on a per-sol basis. We exclude data acquired when dust opacity is $\tau > 1.0$, after Sol 44. Atmospheric dust opacities τ are derived from the Instrument Deployment Camera and Instrument Context Camera (ICC) (Maki et al., 2018) imagery following a procedure described in Spiga et al. (2018). Early in the mission, the visible atmospheric dust opacity values varied widely, from ~ 0.79 shortly after landing to ~ 1.91 at sol 52 ($L_s = 326.$), primarily due to the arrival of a regional dust storm after Sol 40 (Banfield et al., 2020; Viudez-Moreiras et al., 2020). High dust opacity values during dust storm events result in cooler daytime temperatures and warmer nighttime temperatures compared to clear sols, an undesirable configuration to derive soil thermophysical properties because atmosphere modeling assumptions (and associated errors) are magnified under such conditions. As of February 2021, the dust opacity has been monitored for over a full Mars year; we use this record as a KRC input to model the atmosphere several Mars years before landing (the algorithm loops through three Mars years to reach near-surface temperature stability; Kieffer, 2013). When dust opacity is not derived and available for a specific sol, we perform a cubic spline interpolation between the closest values to estimate τ . For the sake of simplicity, and to reduce the processing cost associated with numerical modeling and the fitting procedure, all selected data are binned (averaged) temporally with a resolution of 1 h, so that a

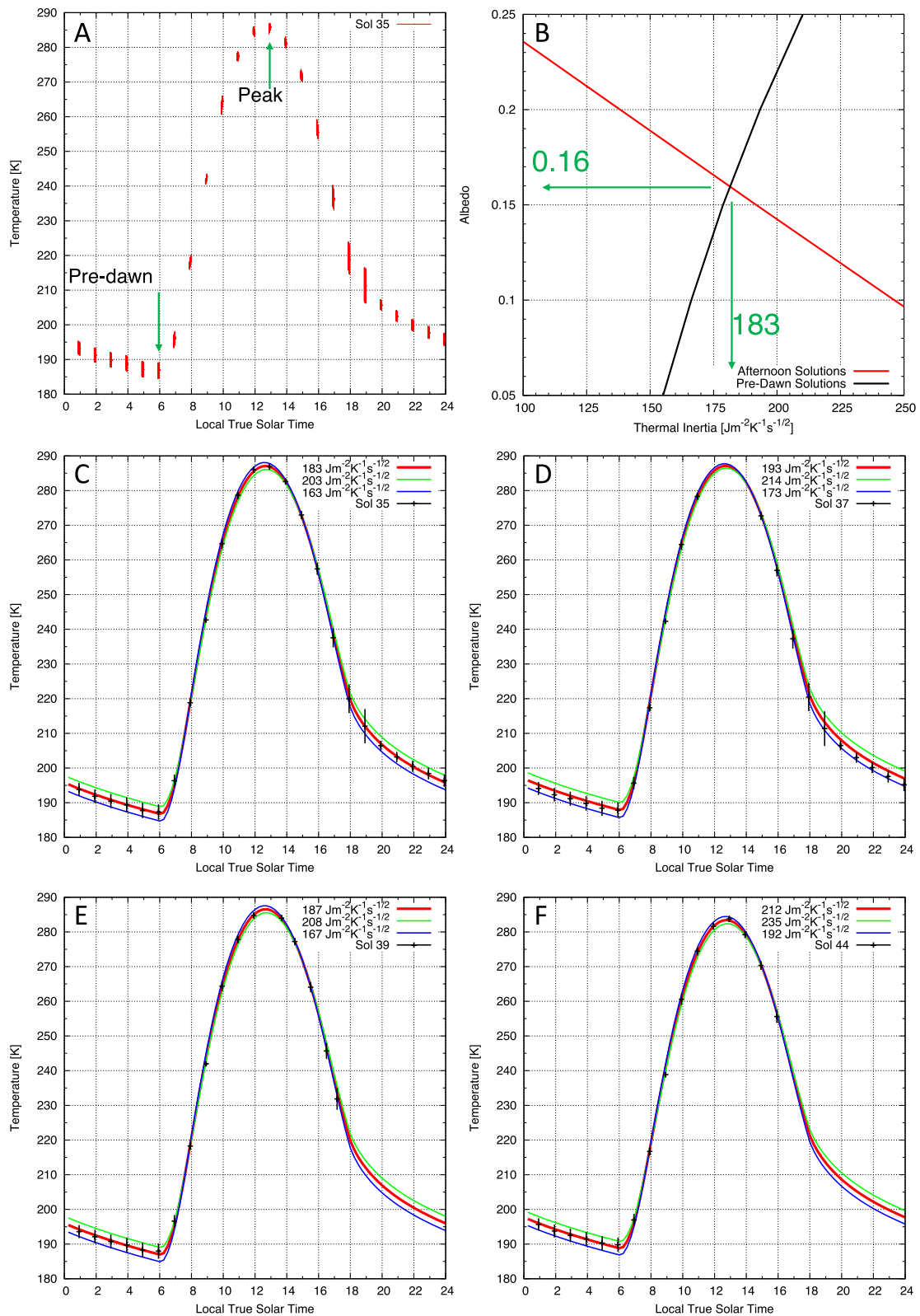


Figure 5.

diurnal cycle is analyzed with a maximum for 24 points per sol (Figure 5), although it is understood that each point is an average of 23 individual observations. In this study, local time is given in local true solar time (LTST), one hour corresponds to 1/24 of a sol, and times are reported with decimal fractions. Similarly, binned (averaged) error bars correspond to the average of the error bars reported with each data point, and are reported as such graphically (Figure 5). Unlike other published approaches, for the fitting of individual sol's diurnal curves, we only consider two distinct local times: one night-time temperature (the coldest, taken near 5.0–6.0 LTST), and one day-side temperature, at the peak time (usually close to 13.0 LTST). This limited selection of two temperatures (as opposed to considering the entire diurnal record) has several advantages: (a) the full amplitude of the diurnal temperature cycle is captured, and best constrains the bulk thermal inertia (Kieffer et al., 1972; Neugebauer et al., 1971), (b) the absolute temperatures (minimum and maximum) values are adequate to constrain the thermometric albedo (Palluconi & Kieffer, 1981), (c) crossover times least diagnostic of the thermophysical properties (e.g., near 7.0 and 15.0 LTST) are ignored, and (d) times of low solar incidence (i.e., 6.0 LTST, and hours following 18.0 LTST) when temperatures are strongly influenced by roughness and heterogeneity when the Sun is near the horizon (Hayne et al., 2017; Putzig & Mellon, 2007b) are not considered. In addition, the accuracy and precision of data acquired near 18.0 LTST is generally negatively impacted by the large temperature differences between the RAD and the surface temperatures; at this local time, RAD switches to the lower reference set point, and errors are therefore reduced after, and maximized before (Mueller, Knollenberg, et al., 2020). For both the daytime and the nighttime observations separately, we invert a model-generated temperature lookup table (LuT) from prescribed albedo (ranging from 0.05 to 0.50) and soil thermal inertia ($100\text{--}300\text{ J m}^{-2}\text{ K}^{-1}\text{ s}^{-1/2}$) in order to identify the families of albedo/thermal inertias able to yield the observed temperatures (Figure 5b). Then we identify the only one albedo/thermal inertia solution able to match both the morning and night observations. The goodness of a fit is evaluated by calculating the root mean square (RMS) between the best model-generated diurnal curve, and the binned diurnal temperature curve using all local times, not just at the pre-dawn and peak temperature times. This approach has the advantage of not being restricted to discretized albedo/thermal inertia solutions unlike regular LuT inversions techniques. In this study, this approach provides excellent fits at all local times at a very small fraction of the computational cost of a full LuT inversion approach. Generally, RMS $\sim 0.5\text{--}0.7\text{ K}$. For some sols, only partial diurnal temperature trends are available; if no data are available within two hours of 13.0 LTST (peak temperature, Figure 5) and pre-dawn, fits are not attempted, and no thermal inertia value is reported. Noise equivalent temperature error bars (mainly caused by the imperfect temperature stabilization of the sensor head due to atmospheric turbulence) are reported for each radiometer measurement and presented in this study in the form of error bars. In addition to deriving the best fit as described above, we also determine the minimum (largest amplitude) and maximum (smallest amplitude) allowable thermal inertia value fitting within the reported error bars.

One weakness of this two-points-only approach manifests itself when the binned pre-dawn and/or peak temperature is not representative of the cooling or warming trends observed before or after. In this case, the fidelity of the fit is evidently not optimized, as encountered on one occurrence, on Sol 37 (Figure 5d) which lacks data near 13.0 LTST and also displays a seemingly warm pre-dawn temperature outlier. Two quantities flag this case as problematic by the fitting procedure: the best fit thermal inertia ($193\text{ J m}^{-2}\text{ K}^{-1}\text{ s}^{-1/2}$) is associated with a noticeably high RMS (e.g., 1.0 K) compared to typical best fit RMS, and the RMS of the lowest thermal inertia fit (within the error bars, i.e., $173\text{ J m}^{-2}\text{ K}^{-1}\text{ s}^{-1/2}$) is lower (e.g., 0.9 K) than the “best fit” RMS, indicating that indeed $173\text{ J m}^{-2}\text{ K}^{-1}\text{ s}^{-1/2}$ is a marginally better solution than $193\text{ J m}^{-2}\text{ K}^{-1}\text{ s}^{-1/2}$.

Figure 5. Graphical example of diurnal temperature fit procedure (a, b), and examples of diurnal fits (c–f). (a) Sol 35, shown for its representative diurnal data distribution and median thermal inertia. Bars indicate unbinned temperature observations, predawn (187.3 K at 5.92 LTST , “pre-dawn”) and peak daytime surface (286.9 K at 12.92 LTST , “peak”) temperatures selected for the fit (see text) ($\tau = 0.79$); (b) Model-generated albedo and thermal inertia solutions for the pre-dawn and peak temperatures, with a unique solution (albedo of 0.16 and a thermal inertia of $183\text{ J m}^{-2}\text{ K}^{-1}\text{ s}^{-1/2}$) matching both the selected pre-dawn (black) and peak (red) temperatures. (c) These steps are repeated to fit the minimum and maximum thermal inertia curves within the reported error bars: binned observations (24 per sol) and best, high, and low thermal inertia model fits within reported error bars, that is, $163, 183, 203\text{ J m}^{-2}\text{ K}^{-1}\text{ s}^{-1/2}$ respectively, yielding RMS of 1.5, 0.4, and 1.7 K, respectively. (d) Sol 37, worst fit (RMS of 1.0 K) of any Sol analyzed yielding $192\text{ J m}^{-2}\text{ K}^{-1}\text{ s}^{-1/2}$ (172 and $214\text{ J m}^{-2}\text{ K}^{-1}\text{ s}^{-1/2}$ upper and lower bound). This case illustrates the limit of using a single predawn observation, as the selected $\sim 6\text{ LTST}$ point may not be representative of the night cooling trend, and the absence of \sim Noon observation limits the leverage to constrain the thermal inertia. Note in this unique pathological case that the lower inertia case yields an RMS of 0.9 K (vs. 2.4 K for the high inertia case) ($\tau = 0.82$); (e) Sol 39, example of excellent fit (RMS of 0.5 K, 1.0 and 1.1 K for the bounding cases) and thermal inertia curves for $167, 187, 208\text{ J m}^{-2}\text{ K}^{-1}\text{ s}^{-1/2}$. The absence of late afternoon data is not detrimental to the retrieval approach ($\tau = 0.87$); (f) Sol 44, good fit (RMS of 0.4 K, vs. 1.0 and 0.9 K for the bounding cases), but highest retrieved thermal inertia values (i.e., $192, 213, 235\text{ J m}^{-2}\text{ K}^{-1}\text{ s}^{-1/2}$ negatively impacted by the high dust opacity and poor modeling performance under dusty conditions) $\tau = 0.95$.

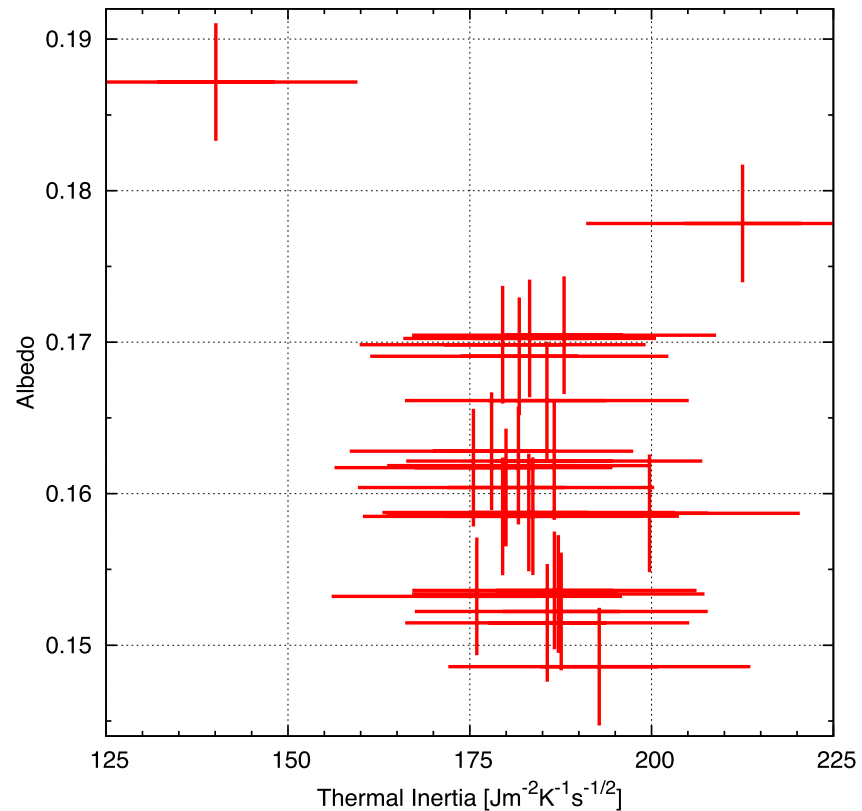


Figure 6. Thermometric albedo versus thermal inertia scattergram. Thermal inertia error bars evaluation is discussed in the text. Albedo error bars arbitrarily set to 1σ (i.e., 0.008).

This unique and pathological case is not filtered out for completeness, as it does not measurably impact the outcome of this analysis that relies on median values.

Over the first 50 sols of the mission analyzed in this study, more than 112,000 measurements have been recorded with 1.7 K (average) and 1.6 K (median) error bars (0.8 K standard deviation) (Mueller, Knollenberg, et al., 2020). Generally, the minimum and maximum thermal inertia are within $\pm 25 \text{ J m}^{-2} \text{ K}^{-1} \text{ s}^{-1/2}$ of the best fit (3σ), corresponding here to $\pm 14\%$ uncertainty. Other quantifiable sources of uncertainties discussed in the literature when deriving thermal inertia values stem from atmospheric dust opacity determination errors, the local slope distribution, and instrument calibration uncertainties (Ferguson et al., 2006). Although significant error might originate in theory from sloped terrains if present, Edwards et al. (2018) concluded that realistic slope uncertainties are typically not an important source of error, presumably even less so in the current study where the terrain around the lander and in the RAD spot is so flat (Figure 3). For this reason, we ignore the local slope as a source of uncertainty. Dust opacity values (Banfield et al., 2020) are reported with errors typically smaller than ± 0.1 , that is, $\sim 14\%$ on average ($\sim 13\%$ median), close to values reported in other studies, for example, up to $\sim 9\%$ (Ferguson et al., 2006). Because these errors are uncorrelated, an estimation of the overall thermal inertia error is estimated by the root sum square of the errors, and evaluated at $\sim 20\%$, largely dominated by the instrumental errors, that is, close to $\pm 25 \text{ J m}^{-2} \text{ K}^{-1} \text{ s}^{-1/2}$ mentioned above based on the allowable fits within the error bars. Thermometric albedo determination errors are not formally evaluated because albedo values are not used to constrain the physical properties of the soil in this study. Figure 6 displays albedo with 0.008 error bars (1σ), shown solely for the sake of clarity and readability.

3. Results and Discussion

3.1. Bulk Properties

A total of 21 sols satisfies the data selection criteria described above. The fitting procedure yields a median and average thermometric albedo of 0.16 (Figure 6), somewhat lower than the TES regional value (i.e., 0.24), but consistent with the $\sim 35\%$ decrease near the lander estimated from high resolution imagery (Golombek, Kass, et al., 2020; Golombek, Warner, et al., 2020). These authors interpret the lower albedo near the lander as the result of a thin dust layer removal, similar to what has been observed near impact blast zones (Daubar et al., 2013, 2014, 2019). This result confirms that an optically thick layer of dust has been removed at the time of landing. The good agreement between the albedo derived from the visible wavelength instruments and our thermometric albedo may be fortuitous, as large differences between the values from these two approaches have been reported throughout the exploration of Mars (Edwards et al., 2018; Ferguson et al., 2006; Morrison et al., 1969; Palluconi & Kieffer, 1981; Walker, 1964).

We derive a median thermal inertia value of $183 \text{ J m}^{-2} \text{ K}^{-1} \text{ s}^{-1/2}$ (average is $185 \text{ J m}^{-2} \text{ K}^{-1} \text{ s}^{-1/2}$, 3σ uncertainty is $25 \text{ J m}^{-2} \text{ K}^{-1} \text{ s}^{-1/2}$) in good agreement with a pre-landing assessment using THEMIS data, that is, $166 \text{ J m}^{-2} \text{ K}^{-1} \text{ s}^{-1/2}$ (Golombek, Kass, et al., 2020; Golombek, Warner, et al., 2020), Figures 1 and 6. The good agreement between the orbital pre-landing value, and the post-landing surface-based value confirms that the dust layer blown away by the pulsing retro-rockets was thermally thin.

Assuming a soil density of $\sim 1,300 \text{ kg m}^{-3}$ (porosity $\sim 55\%$, based on ideal laboratory samples (Presley & Christensen, 1997) and references in Morgan et al. (2018), with an uncertainty of 200 kg m^{-3} toward high densities) and specific heat of $630 \text{ J kg}^{-1} \text{ K}^{-1}$ (from Vu et al., 2019 and references in Morgan et al., 2018), we calculate a soil thermal conductivity of $0.041 \pm 0.013 \text{ W m}^{-1} \text{ K}^{-1}$ in excellent agreement with an *in situ* thermal conductivity determination by the lander (Grott, Spohn, Knollenberg, Krause, Hudson, et al., 2021; Grott, Spohn, Knollenberg, Krause, Nagihara, et al., 2021) and observations of the surface during Phobos transits (Mueller, Grott, et al., 2020; Mueller et al., 2021). This conductivity value under Mars conditions of atmospheric pressure and gas composition indicates that 85%–95% of the soil grains are smaller than $140 \mu\text{m}$ based on laboratory analogs (Presley & Christensen, 1997; Presley & Craddock, 2006). It does not exclude the existence of dust aggregates cemented by small amounts of cement (but not by electrostatic forces, which have no impact on thermal conductivity) (Greeley, 1979) that would behave thermally like fine sand. Numerical modeling suggests that the lower temperatures encountered on Mars compared to the laboratory (Presley & Christensen, 1997) may result in a modest underestimation of the grain sizes (Piqueux & Christensen, 2009a, 2011, 2011), which would nevertheless correspond to very fine to fine sand. Such particulate material would be consistent with the geological analysis of the terrains surrounding the lander showing that the InSight lander is located in a crater filled with aeolian material (Grant et al., 2020; Warner et al., 2020).

During the 21-sol study period, two thermal inertia outliers are noted, on sols 16 ($140 \text{ J m}^{-2} \text{ K}^{-1} \text{ s}^{-1/2}$) and 44 ($213 \text{ J m}^{-2} \text{ K}^{-1} \text{ s}^{-1/2}$). Measurements on sol 16 correspond to the first acquisitions by the RAD after landing, and the reason for the low inertia value (i.e., unique temperatures) are not understood. Sol 44 corresponds to a time when the atmospheric dust opacity increases near $\tau = 1$ as a result of the arrival of a regional dust storm (Banfield et al., 2020). The physical and optical properties of the dust present in the atmosphere during large dust events is different than inter-dust storm atmospheric dust (Clancy et al., 2010; Elteto & Toon, 2010), so that the parameters used for the modeling (Table 1) results in low fidelity fits. Similarly, sol-to-sol albedo variations are not further investigated in this study. Over the relatively short period of time studied for this work, we notice no correlation with weather variability as presented in Spiga et al. (2020) in terms of wind speed, direction, and air temperature (their Figures 2 and 8) versus albedo or thermal inertia variability. This absence of correlation is also consistent with the low sensible heat flux value (i.e., atmosphere/surface heat transfer through conduction) relative to other fluxes (Spiga et al., 2020) modeled in KRC. Finally, the sol-to-sol thermometric albedo variability does not correlate with known soil variability identified in imagery or solar panels currents (Lorenz et al., 2020).

Similar temperature observations and numerical analysis have yielded comparable thermal inertia values on well-sorted aeolian material at the Namib and Bagnold dunes in Gale crater, for example, $170\text{--}180 \text{ J m}^{-2} \text{ K}^{-1} \text{ s}^{-1/2}$ (Vasavada et al., 2017) and $180\text{--}200 \text{ J m}^{-2} \text{ K}^{-1} \text{ s}^{-1/2}$ (Edwards et al., 2018), respectively. At

both locations, the THEMIS orbitally derived thermal inertia values (e.g., 250–315 and 240 $\text{J m}^{-2} \text{K}^{-1} \text{s}^{-1/2}$ on average) were noticeably higher than those derived from the ground, possibly because of subpixel mixing with nearby high thermal inertia bedrock-type material. Results from microscope imagery analysis were generally consistent with thermally derived grain sizes and provide additional in situ confirmation of laboratory parametrizations (Presley & Christensen, 1997). No indication of cohesion or cementation were observed in visible imagery, as expected with active sand dunes, including within tracks created by the rover's wheels. In addition, the thermal inertia values of aeolian bedforms observed by Mini-TES in Bonneville and Endurance craters were also nearing 200 $\text{J m}^{-2} \text{K}^{-1} \text{s}^{-1/2}$ (Ferguson et al., 2006), although these locations displayed evidence of armoring that do not seem to impact the apparent thermal properties of the soil at these locations. At other locations in Gusev crater, Ferguson et al. (2006) derived thermal inertias values ranging from 100 to 200 $\text{J m}^{-2} \text{K}^{-1} \text{s}^{-1/2}$ for soil-infilled hollows that were not associated with eolian bedforms. Mini-TES and THEMIS measurements of dark soils traversed by the Opportunity rover at Meridiani Planum also have displayed thermal inertia values that correspond to cohesionless fine to very fine sand (Ferguson et al., 2006; Golombek et al., 2014). These results at locations other than Homestead hollow indicate that thermal inertia values nearing 180 $\text{J m}^{-2} \text{K}^{-1} \text{s}^{-1/2}$ are not dissimilar to other crater infillings observed elsewhere on Mars, and close to values derived for well-sorted aeolian bedforms.

3.2. Layering

While excellent fits are obtained within error bars for homogeneous soil configurations (Figure 5), material layering could still be present: First, the lower albedo zone around the lander formed at the time of touchdown indicates that an optically thick layer (but thermally thin at the diurnal cycle time scale) of fine dust was originally present and has been at least partially removed (Golombek, Warner, et al., 2020). Surface cooling during Phobos transits (Mueller, Grott, et al., 2020; Mueller et al., 2021; Stahler et al., 2020) is also consistent with an up to a 4 mm thick top layer characterized by a relatively low conductivity and thermal inertia, for example, $\sim 75 \text{ J m}^{-2} \text{K}^{-1} \text{s}^{-1/2}$ on a higher thermal inertia soil with $\sim 200 \text{ J m}^{-2} \text{K}^{-1} \text{s}^{-1/2}$ (Mueller, Grott, et al., 2020; Mueller et al., 2021). Finally, images of the HP³ mole support structure feet after the first set of hammering on sol 92 is most consistent with a ~ 1 cm (or more) thick layer of loose material resting on stronger, more cohesive material estimated to reach at least 10 cm in thickness (Figure 4) (Golombek, Warner, et al., 2020; Hudson et al., 2020). In short, near-surface soil layering is present, but we see no signature in the diurnal temperature data.

Qualitatively, near-surface heterogeneity within the diurnal skin depth can be identified by differential phasing at the local times of most pronounced warming/cooling compared to a homogeneous soil. Generally, a thin low thermal inertia layer on top of higher thermal inertia material results in faster morning warming, as well as faster cooling in the afternoon. This type of configuration has been observed and characterized with temperature data (Vasavada et al., 2017), and the ability to adequately retrieve the thickness and thermal inertia of the layers is driven by the thermal inertia contrast between the different materials, as well as the depth of the interface. If the top layer is too thin or too thick, or its thermal properties too close to those of the lower layer, the diurnal temperature trends are not sufficiently impacted for proper characterization. Similarly, high thermal inertia layers on top of low thermal inertia material have been observed on the ground, for example, in the case of desert pavement or exposed duricrust, and characterized using diurnal temperature trends (Edwards et al., 2018; Ferguson et al., 2006; Hamilton et al., 2014; Vasavada et al., 2017). Note that this type of layered soil characterization is only possible when resolving the full diurnal temperature cycle, that is, cannot be done from orbit with sun-synchronous assets except when leveraging rare Phobos eclipses (Betts et al., 1995; Piqueux & Christensen, 2012).

Quantitatively, we aim at characterizing the realm of subsurface heterogeneity that would yield low RMS fits through a parametric study assuming two-layer soil with varying top layer thickness (d_{top} 100 μm to 0.1 m) and thermal inertia (TI_{top} 50–600 $\text{J m}^{-2} \text{K}^{-1} \text{s}^{-1/2}$), on a semi-infinite bottom layer material ($\text{TI}_{\text{bot}} = 180, 190,$ and 200 $\text{J m}^{-2} \text{K}^{-1} \text{s}^{-1/2}$, Figure 7a). We note that other TI_{bot} values quickly yield large RMS, regardless of soil layering properties, and are not further discussed. Some families of model configurations are numerically unstable without significant *ad hoc* tuning and increased processing time (e.g., when extremely thin layers and high thermophysical contrast with adjacent material) and are generally unphysical (when a layer thickness is smaller than the individual grain sizes that form it); we have not further investigated them and the

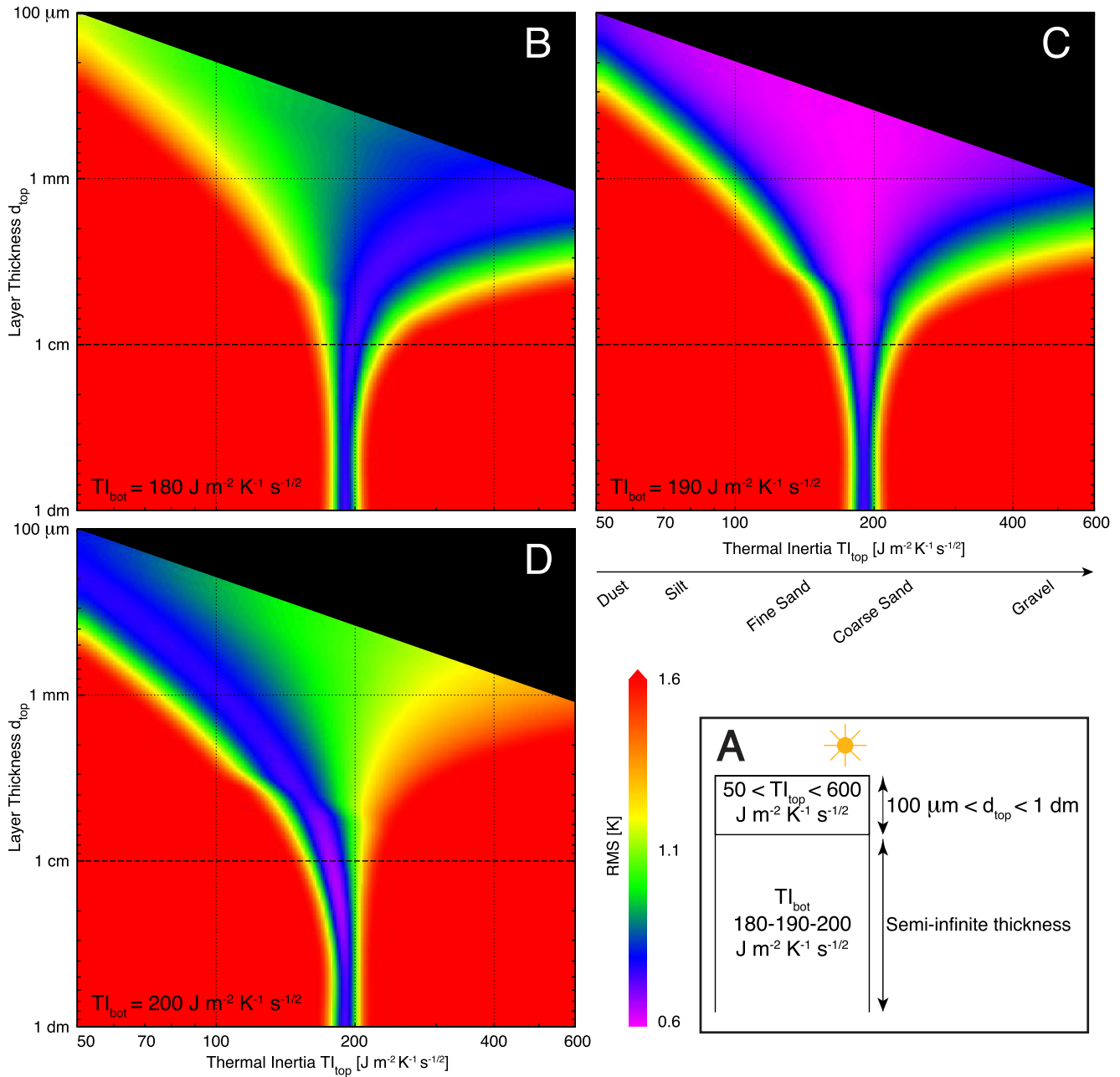


Figure 7. (a) Schematics of the thermal model configuration and nomenclature. (b–d) RMS between observed temperatures on sol 35 (see Figures 5 and 6) and a modeled layered soil with varying top layer thickness (Y axis, d_{top}), top layer thermal inertial (X axis, TI_{top}), and bottom layer thermal inertia TI_{bot} . (b) $TI_{bot} = 180 \text{ J m}^{-2} \text{ K}^{-1} \text{ s}^{-1/2}$; (c) $TI_{bot} = 190 \text{ J m}^{-2} \text{ K}^{-1} \text{ s}^{-1/2}$; (d) $TI_{bot} = 200 \text{ J m}^{-2} \text{ K}^{-1} \text{ s}^{-1/2}$. Horizontal dashed lines at $d_{top} = 1 \text{ cm}$ provides a marker consistent with the observation of loose material at the surface (see Figure 4a). Approximate equivalence between thermal inertia and grain sizes given under (c), assuming no cementation.

relevant domains are shown in black in Figures 7b–7d. We report that the vast majority of the layered cases yield large RMS, for example, $RMS > 1.6 \text{ K}$, red in Figure 7. These cases are not further considered and discussed here. Intermediate cases where $\sim 0.7 < RMS < 1.6 \text{ K}$ (blue to orange in Figures 7b–7d) are associated with numerically acceptable fits (i.e., temperature generally fall within measurement error bars), but they still correspond to noticeably degraded fits compared to optimized homogeneous soil configurations. These cases associated with blue-orange hues in Figures 7b–7d are not further considered for discussion. Finally, some families of fits are typically as good or marginally better than with homogeneous configurations (e.g., $RMS \sim 0.5\text{--}0.7 \text{ K}$, purple in Figures 7b–7d), and they can be considered equally robust at matching the

temperature observations. These cases correspond to the layered soil configurations realistically present from a numerical point-of-view, and further discussed in this section of the study.

First, we investigate the hypothetical case of a low bottom layer thermal inertia material, that is, $TI_{\text{bot}} = 180 \text{ J m}^{-2} \text{ K}^{-1} \text{ s}^{-1/2}$ compared to the best fit thermal inertia mentioned earlier in the study. Figure 7b shows that this configuration requires a thick (i.e., $d_{\text{top}} > 1 \text{ mm}$) high thermal inertia (i.e., $TI_{\text{top}} > 300 \text{ J m}^{-2} \text{ K}^{-1} \text{ s}^{-1/2}$, ideally closer to $600 \text{ J m}^{-2} \text{ K}^{-1} \text{ s}^{-1/2}$) top layer in order to obtain acceptable fits based on RMS values. This notion of a mm thick d_{top} and a high TI_{top} thermal inertia layer (i.e., composed of larger grains forming an armor, or a more cemented uppermost horizon) is inconsistent with the geological analysis of the soil structure that shows loose upper material (Golombek, Warner, et al., 2020; Golombek, Williams, et al., 2020), and can be discarded.

The soil configuration with the highest density probability of a low RMS is shown in Figure 7c: with $TI_{\text{bot}} = 190 \text{ J m}^{-2} \text{ K}^{-1} \text{ s}^{-1/2}$ (just a few $\text{J m}^{-2} \text{ K}^{-1} \text{ s}^{-1/2}$ higher than the best homogeneous soil fit, i.e., $183 \text{ J m}^{-2} \text{ K}^{-1} \text{ s}^{-1/2}$), a wide range of top layer material inertias TI_{top} and thicknesses d_{top} can yield acceptable fits (RMS $\sim 0.6 \text{ K}$). In particular, a top layer with $d_{\text{top}} = \sim 200\text{--}300 \text{ }\mu\text{m}$ made of very fine Mars dust ($TI_{\text{top}} = 75 \text{ J m}^{-2} \text{ K}^{-1} \text{ s}^{-1/2}$), or a thicker top layer (i.e., $d_{\text{top}} \leq 3 \text{ mm}$) made of coarser material ($TI_{\text{top}} = 150 \text{ J m}^{-2} \text{ K}^{-1} \text{ s}^{-1/2}$ corresponding to $\sim 70 \text{ }\mu\text{m}$ grains and smaller Presley & Christensen, 1997; Presley & Craddock, 2006; Presley et al., 2009), the latter being the minimum grain size observed to saltate on Mars (Sullivan et al., 2005, 2008; Weitz et al., 2018), would remain unnoticed when fitting diurnal temperature observations (Figure 7). We note that a top layer with $TI_{\text{top}} = 75 \text{ J m}^{-2} \text{ K}^{-1} \text{ s}^{-1/2}$ suggested by eclipse cooling observations would remain within 1.5 K RMS as long as its thickness $d_{\text{top}} < 600 \text{ }\mu\text{m}$. We conclude that a bottom layer characterized by $TI_{\text{bot}} = 190 \text{ J m}^{-2} \text{ K}^{-1} \text{ s}^{-1/2}$, typical of aeolian material, and a mm (or less) thin layer of fines forms a soil configuration compatible with the far RAD temperature observations.

Figure 7d illustrates the goodness of fits when considering a relatively high bottom material thermal inertia (i.e., $TI_{\text{bot}} = 200 \text{ J m}^{-2} \text{ K}^{-1} \text{ s}^{-1/2}$, noticeably higher than with the best homogeneous soil fit, i.e., $183 \text{ J m}^{-2} \text{ K}^{-1} \text{ s}^{-1/2}$). In this configuration, a top low thermal inertia layer (i.e., $TI_{\text{top}} < 100 \text{ J m}^{-2} \text{ K}^{-1} \text{ s}^{-1/2}$) is numerically possible as long as d_{top} remains thin (i.e., $d_{\text{top}} < 2 \text{ mm}$ in thickness). The top layer thickness d_{top} must be significantly thinner as the thermal inertia contrast between TI_{top} and TI_{bot} increases. In other words, excellent fits characterized by blue domains in Figure 7d can be obtained with a low thermal inertia layer at the top as long as it does not exceed a couple of mm in thickness.

Next, we investigate the specific configuration illustrated in Figure 4a where a loose upper layer ($d_{\text{tot}} \sim 1 \text{ cm}$) is identified on top of a cohesive semi-infinite lower layer. A horizontal dashed line marks $d_{\text{tot}} = 1 \text{ cm}$ in Figures 7b–7d. To remain within low RMS domains, Figure 7 shows that TI_{top} cannot have a fundamentally different thermal inertia than TI_{bot} . In other words, $TI_{\text{top}} \sim TI_{\text{bot}}$ if $d_{\text{top}} \sim 1 \text{ cm}$. This result is rather intuitive given the diurnal skin depth for $\sim 180\text{--}200 \text{ J m}^{-2} \text{ K}^{-1} \text{ s}^{-1/2}$ material, that is, $\sim 4 \text{ cm}$, and comparable to $d_{\text{tot}} = 1 \text{ cm}$. This modeling constraint on the upper layer properties has an important implication for the interpretation of the soil structure: the top loose layer identified in imagery (Figure 4a) has similar thermophysical properties as the underlying cohesive layer, which implies that either the cohesion of the bottom layer does not stem from the presence of a cementing phase, or that its volumetric quantity is too low to impact the bulk conductivity. Yet, models and laboratory observations have shown that extremely small amounts of cements have a very large thermal conductivity effect (Mellon et al., 2008; Piqueux & Christensen, 2009b; Presley et al., 2009), especially compared to the mechanical properties (Piqueux, 2009), although in the latter case only qualitative observations are available. With a layered configuration, these modeling results suggest that next to no cementing phase is present.

Finally, a highly cemented soil ($TI_{\text{bot}} = 600 \text{ J m}^{-2} \text{ K}^{-1} \text{ s}^{-1/2}$, corresponding to $\sim 1\%$ cement; Mellon et al., 2008) that would potentially match geological observation (Figure 4b) could be present, but it would have to be buried below nearly two diurnal skin depth or more (i.e., 8 cm with a typical apparent thermal inertia of $183 \text{ J m}^{-2} \text{ K}^{-1} \text{ s}^{-1/2}$) of lower thermal inertia material in order to remain unnoticeable from surface temperature observations. Analysis of active soil heating and associated thermal conductivity measurement of the top $\sim 40 \text{ cm}$ of soil excludes this configuration (Grott, Spohn, Knollenberg, Krause, Hudson, et al., 2021; Grott, Spohn, Knollenberg, Krause, Nagihara, et al., 2021).

Overall, beneath the far RAD spot, we conclude that a possible subsurface configuration consistent with these results corresponds to a low conductivity top layer a few hundreds of microns to mm in thickness, on top of a nearly cohesionless fine sand layer at least 4 cm thick. These results will become increasingly valuable to understand the subsurface structure of the Martian soil when interpreted in conjunction with the Phobos transits cooling results (Mueller, Grott, et al., 2020; Mueller et al., 2021), and the deeper in situ conductivity measurements by the mole (Grott, Spohn, Knollenberg, Krause, Hudson, et al., 2021; Grott, Spohn, Knollenberg, Krause, Nagihara, et al., 2021).

3.3. Duricrust

Analysis of imagery further into the hollow interior (e.g., Figure 4b; Golombek, Warner, et al., 2020) is strongly suggestive of the presence of a cementing phase within the soil, forming a duricrust. A duricrust is also most consistent with the measured mechanical properties of the soil (Marteau et al., 2021), and could explain the resistance to the mole penetration. In a duricrust, cements contribute to increase the effective contact surface area between grains and transform a poorly conductive discontinuous medium into a continuous high-conductivity solid material. As a result, very small amounts of cements have a significant impact on bulk soil thermal conductivities and can result in a gross overestimation of the typical grain sizes (Piqueux & Christensen, 2009a, 2009b). Using the parameterization provided by Piqueux and Christensen (2009a, 2009b) and laboratory measurements, we find that a bulk soil thermal conductivity of $0.041 \text{ W m}^{-1} \text{ K}^{-1}$ is difficult to obtain with any measurable volume/mass of cementing material: even $\sim 1\%$ of cement would raise the bulk conductivity by one order of magnitude and the apparent thermal inertia to $\sim 600 \text{ J m}^{-2} \text{ K}^{-1} \text{ s}^{-1/2}$ (Mellon et al., 2008), a value far greater than derived from the RAD measurements. Similarly, laboratory measurements show that such low thermal inertia values are most consistent with very small amount of cement ($\ll 1\%$) (Presley et al., 2009). As a result, the interpretation of the thermal data that excludes or severely limits the amount of cement in the soil is difficult to reconcile with all the other evidence arguing for the presence of a duricrust.

Cemented material conductivity models rely on simplifying assumptions (in particular packing style, absence of grain roughness, and distribution of cements) that only provide an approximation for the amount of cement and overall effect on the derived grain size. In particular, the estimation of cement amounts in this study rely on Piqueux and Christensen (2009b) assumption of bonding phases concentrated in the inter-grain regions, but if cement coats individual grains (as opposed to forming menisci at the inter-grain regions similar to “thin films” with liquids, see auxiliary material in Edwards & Piqueux, 2016), the amount of cement could be somewhat larger than reported here, and only the cementing phase located in the inter-grain regions contributes to the enhanced conductivity and mechanical strength. Nonetheless, the very limited cementation inferred from the thermal data at the far RAD spot appears to contradict the geological analysis of the pits in Homestead hollow (Figure 4b), just a few meters away (Figure 2).

We cannot exclude that lateral variation in soil sedimentology and cementation exist across the local landing area, so that the soil material characterized at the far RAD spot is not fully representative of the material exposed in the pits. The RAD spot is located along the northwest edge of the Homestead hollow impact structure, likely near or on the degraded crater rim (Grant et al., 2020; Warner et al., 2020) where surface material might be less sheltered than within the hollow. Near the edge of the hollow, at the far RAD spot, the surface clast-size distribution is closer to the coarser, impact-fragmented inter-crater plains that surround Homestead hollow (Golombek et al., 2018; Golombek, Warner, et al., 2020; Golombek, Williams, et al., 2020), where surface soils are dominated by sand, but where the frequency of pebbles and cobbles is also higher (Figure 2). In contrast, $\sim 6 \text{ m}$ away from the RAD spot, the mole pit is more centrally located, entirely within better-sorted, sand-sized, hollow fill materials that have a lower abundance of pebble and cobble-size materials. This difference in clast size distribution reflects the gentler, maybe more stable evolution of the material inside the hollow compared to the edge, at the RAD spot. For a Homestead hollow-size depression ($\sim 27 \text{ m}$ diameter), with a maximum landscape retention age of $\sim 400\text{--}700 \text{ Myr}$ (Warner et al., 2020), quantitative landscape evolution indicates that the fill rate declines non-linearly to near zero within just the first $\sim 100 \text{ Myr}$ of crater exposure (Grant et al., 2020; Sweeney et al., 2018; Warner et al., 2020). From that point in time, the soil centrally located inside the hollow remains relatively stable for the next few hundred million years, allowing long-term atmospheric water vapor diffusion and the development of a mature duricrust.

The observed thickness of the cohesive soils in the mole hole and retro-rocket pits has been attributed to this stability (Warner et al., 2020). In other words, the InSight lander, and therefore our RAD and visual soil observations straddle an important boundary between uniquely stabilized sand-dominated and thicker crater fill conducive to duricrust formation near the mole pit on one hand, and more reworked/less stable/more exposed material at the margin of the hollow at the RAD spot on the other hand. However, even given this geologic context, the lateral cementation gradients within the hollow must remain modest enough in thickness and/or degree of cementation (or buried enough) given the excellent agreement between the *in-situ* conductivity measurement performed by the mole (Grott, Spohn, Knollenberg, Krause, Hudson, et al., 2021; Grott, Spohn, Knollenberg, Krause, Nagihara, et al., 2021) and the values derived in this work at the RAD spot, several meters away.

For completeness, we mention here that other mechanisms could conceivably increase internal cohesion without involving cementation, that is, without increasing the contact area between individual grains that would result in high thermal conductivities or inertia. They involve electrostatic forces (Greeley, 1979), geometrical and mechanical properties of grain size mixtures (Statham, 1974), or the effect of individual grain roughness on mechanical properties (Pohlman et al., 2006). These mechanisms are not further discussed in this study because not associated with observables by the InSight payload.

Together, these results suggest that the upper few cm of the Martian soil at the more distant RAD spot than the InSight lander and the mole are only very slight cemented at most, in contrast with evidence of higher cohesion (Marteau et al., 2021) and cementation discussed elsewhere (Golombek et al., 2018; Golombek, Warner, et al., 2020). This characterization is still broadly consistent with inferences drawn from the more central interior of the hollow, a pre-landing regional assessment (Golombek, Kass, et al., 2020), and hypotheses pertaining to landscape evolution on Mars (Sweeney et al., 2018).

4. Conclusions

We present an analysis of the InSight lander HP³ far radiometer data acquired during the first 50 sols of the mission, during which 21 one hour-binned diurnal temperatures cycles have been recorded. This work demonstrates the ability of thermal models to emulate diurnal surface temperatures on Mars with very high fidelity at all local times. Owing to its fixed platform, thoroughly studied nearby geology, and well-characterized footprint on an extensively studied surface, InSight HP³ RAD data provide a unique opportunity to constrain soil properties and ground-truth orbital predictions of soil micro-to-macro scale properties:

1. Best fits to the measured diurnal temperature curves are obtained with a surface thermometric albedo of 0.16, in excellent agreement with the regional pre-landing value of 0.24 darkened by ~35% as determined from orbital data as a result of dust removal. The albedo is predicted to increase over the duration of the mission following the seasonal and interannual dust deposition/removal cycle.
2. Best fits to the diurnal temperature curves are obtained with a soil thermal inertia of $183 \pm 25 \text{ J m}^{-2} \text{ K}^{-1} \text{ s}^{-1/2}$ (typical RMS = 0.5–0.7 K), again in excellent agreement with a pre-landing orbital determination and data analysis of Phobos transits.
3. The derived thermal conductivity of the soil, that is, $0.041 \pm 0.013 \text{ W m}^{-1} \text{ K}^{-1}$ is only consistent with a very small amount of cementing phase that would only be able to generate a very weak unquantified mechanical induration.
4. The corresponding material is consistent with uncemented 140 μm (or smaller) fine sand, compatible with the evidence that Homestead hollow is a degraded crater filled by aeolian activity.
5. The timing of the peak temperature in the early afternoon, and the overall shape of the diurnal curves are reproduced with simple soil models and argues for homogeneous material properties at the scale of a diurnal skin depth, that is, ~4 cm.
6. However, soil thermophysical heterogeneity (i.e., internal layering) could be present and undetected if associated with thin-enough and/or low-enough thermophysical contrast. For example, a ~300 μm thick layer of typical $50 \text{ J m}^{-2} \text{ K}^{-1} \text{ s}^{-1/2}$ dust, or less than a few mm of $100 \text{ J m}^{-2} \text{ K}^{-1} \text{ s}^{-1/2}$ fines would yield an acceptable RMS fit with the proposed approach and remain consistent with the analysis of Phobos transit data (Mueller, Grott, et al., 2020; Mueller et al., 2021). Similarly, a buried and highly indurated layer associated with $600 \text{ J m}^{-2} \text{ K}^{-1} \text{ s}^{-1/2}$ (~1% cement) below just a few cm of fine sand or more would remain

- unidentified with our approach but is excluded by other measurements (Grott, Spohn, Knollenberg, Krause, Hudson, et al., 2021; Grott, Spohn, Knollenberg, Krause, Nagihara, et al., 2021).
7. Geological and mechanical analyses have concluded that a duricrust requiring non-trivial amounts of cements is present under the lander, in apparent contradiction with the RAD data analysis indicative of low cementation. This discrepancy may partially stem from the differential evolution of the material toward the center of the hollow, that is, under the lander, associated with uniquely stabilized sand-dominated crater fill that could have developed a mature duricrust. In contrast, the less mature soil at the edge of the hollow, where the RAD measurements are performed, maybe closer to the intra-crater, less evolved material. Nonetheless, a direct thermal conductivity measurement (Grott, Spohn, Knollenberg, Krause, Hudson, et al., 2021) suggests that the soil thermophysical properties are similar at the RAD spot and near the lander.
 8. Future thermophysical work could help refine our understanding of the soil properties at Homestead hollow. First, the analysis of the near RAD data could unveil shallow soil thermophysical properties gradients at the lateral scale of just a few meters. Second, the annual temperature trends could inform deeper soil properties at a vertical scale comparable to TEM-A conductivity measurements (Grott, Spohn, Knollenberg, Krause, Hudson, et al., 2021; Grott, Spohn, Knollenberg, Krause, Nagihara, et al., 2021). Finally, the importance of inter-grain cementation can be quantified when leveraging seasonal pressure trends, as the thermal inertia (or conductivity) of cemented material is modeled to remain mainly independent of atmospheric pressure (Piqueux & Christensen, 2009b), in contrast with the thermal properties of unconsolidated material (Piqueux & Christensen, 2009a) that should oscillate throughout the Mars year.

The characterization and interpretation of just a few diurnal temperature curves acquired on a surface near the InSight lander and thermophysical characterization work performed by others (Grott, Spohn, Knollenberg, Krause, Hudson, et al., 2021; Grott, Spohn, Knollenberg, Krause, Nagihara, et al., 2021; Mueller, Grott, et al., 2020; Mueller et al., 2021) provides a significant amount of information on the uppermost soil properties. These results rely on and complement the findings stemming from local geological analysis.

Data Availability Statement

Data presented in this manuscript is publicly available at the Planetary Data System. All radiometer data used in this study is publicly available on the PDS (<https://pds-geosciences.wustl.edu/missions/insight/hp3rad.htm>). The KRC numerical model (Kieffer, 2013, version 3.6.5) is publicly distributed here: <http://krc.mars.asu.edu/svn/listing.php>. This study is *InSight Contribution Number 148*.

Acknowledgments

The design, building of and research into the HP³ has been supported by the German Aerospace Center DLR, NASA, the Austrian Academy of Science ÖAW, and the Polish Academy of Science PAN. Part of this work was performed at the Jet Propulsion Laboratory, California Institute of Technology, under a contract with NASA. US government support acknowledged.

References

- Arvidson, R. E., Anderson, R. C., Bartlett, P., Bell, J. F., Christensen, P. R., Chu, P., et al. (2004). Localization and physical properties experiments conducted by Opportunity at Meridiani Planum. *Science*, *306*, 1730–1733. <https://doi.org/10.1126/science.1104211>
- Arvidson, R. E., Anderson, R. C., Bartlett, P., Bell, J. F., III, Balney, D., Christensen, P. R., et al. (2004). Localization and physical properties experiments conducted by Spirit at Gusev Crater. *Science*, *305*, 821–824. <https://doi.org/10.1126/science.1099922>
- Arvidson, R. E., Guinness, E. A., Dale-Bannister, M. A., Adams, J., Smith, M., Christensen, P. R., & Singer, R. B. (1989). Nature and distribution of surficial deposits in Chryse Planitia and vicinity, Mars. *Journal of Geophysical Research*, *94*, 1573–1587. <https://doi.org/10.1029/jb094ib02p01573>
- Arvidson, R. E., Squyres, S. W., Anderson, R. C., Bell, J. F., Blaney, D., Brückner, J., et al. (2006). Overview of the spirit mars exploration rover mission to Gusev Crater: Landing site to Backstay Rock in the Columbia Hills. *Journal of Geophysical Research*, *111*, E02S01. <https://doi.org/10.1029/2005JE002499>
- Banerdt, W. B., Smrekar, S. E., Banfield, D., Giardini, D., Golombek, M., Johnson, C. L., et al. (2020). Initial results from the InSight mission on Mars. *Nature Geoscience*, *14*, 183–189. <https://doi.org/10.1038/s41561-020-0544-y>
- Banfield, D., Rodriguez-Manfredi, J. A., Russell, C. T., Rowe, K. M., Leneman, D., Lai, H. R., et al. (2019). InSight auxiliary payload sensor suite (APSS). *Space Science Reviews*, *215*(1), 1–33. <https://doi.org/10.1007/s11214-018-0570-x>
- Banfield, D., Spiga, A., Newman, C., Forget, F., Lemmon, M., Lorenz, J., et al. (2020). The atmosphere of Mars as observed by InSight. *Nature Geoscience*, *19*, 190–198. <https://doi.org/10.1038/s41561-020-0534-0>
- Betts, B. H., Murray, B. C., & Svitek, T. (1995). Thermal Inertias in the upper millimeters of the Martian surface derived using Phobos shadow. *Journal of Geophysical Research*, *100*(E3), 5285–5296. <https://doi.org/10.1029/95je00226>
- Binder, A. B., Arvidson, R. E., Guinness, E. A., Jones, K. L., Morris, E. C., Mutch, T. A., et al. (1977). The geology of the Viking Lander 1 site. *Journal of Geophysical Research*, *82*, 4439–4451. <https://doi.org/10.1029/js082i028p04439>
- Christensen, P. R. (1986). The spatial distribution of rocks on Mars. *Icarus*, *68*, 217–238. [https://doi.org/10.1016/0019-1035\(86\)90020-5](https://doi.org/10.1016/0019-1035(86)90020-5)

- Christensen, P. R., Bandfield, J. L., Hamilton, V. E., Ruff, S. W., Kieffer, H. H., Titus, T. N., et al. (2001). The Mars global surveyor thermal emission spectrometer experiment: Investigation description and surface science results. *Journal of Geophysical Research*, *106*(E10), 23823–23871. <https://doi.org/10.1029/2000JE001370>
- Christensen, P. R., Jakosky, B. M., Kieffer, H. H., Malin, M. C., McSweeney, Jr., H. Y., Neelson, K., et al. (2004). The thermal emission imaging system (THEMIS) for the Mars 2001 Odyssey Mission. *Space Science Reviews*, *110*, 85–130. <https://doi.org/10.1023/b:spac.0000021008.16305.94>
- Christensen, P. R., Mehall, G. L., Silverman, S. H., Anwar, S., Cannon, G., Gorelick, N., et al. (2003). The miniature thermal emission spectrometer for the Mars exploration rovers. *Journal of Geophysical Research*, *108*, 8064. <https://doi.org/10.1029/2003JE002117>
- Clancy, R. T., Wolff, M. J., Whitney, B. A., Cantor, B. A., Smith, M. D., & McConnochie, T. H. (2010). Extension of atmospheric dust loading to high altitudes during the 2001 Mars dust storm: MGS TES limb observations. *Icarus*, *207*(1), 98–109. <https://doi.org/10.1016/j.icarus.2009.10.011>
- Daubar, I. J., Atwood-Stone, C., Byrne, S., McEwen, A. S., & Russell, P. S. (2014). The morphology of small fresh craters on Mars and the Moon. *Journal of Geophysical Research: Planets*, *119*(12), 2620–2639. <https://doi.org/10.1002/2014je004671>
- Daubar, I. J., Banks, M. E., Schmerr, N. C., & Golombek, M. P. (2019). Recently formed crater clusters on Mars. *Journal of Geophysical Research: Planets*, *124*(4), 958–969. <https://doi.org/10.1029/2018je005857>
- Daubar, I. J., McEwen, A. S., Byrne, S., Kennedy, M. R., & Ivanov, B. (2013). The current Martian cratering rate. *Icarus*, *225*(1), 506–516. <https://doi.org/10.1016/j.icarus.2013.04.009>
- Edgett, K. S., Yingst, R. A., Ravine, M. A., Caplinger, M. A., Maki, J. N., Ghaemi, F. T., et al. (2012). Curiosity's Mars Hand Lens Imager (MAHLI) investigation. *Space Science Reviews*, *170*(1–4), 259–317. <https://doi.org/10.1007/s11214-012-9910-4>
- Edwards, C. S., Christensen, P. R., & Hill, J. (2011). Mosaicking of global planetary image datasets: 2. Modeling of wind streak thicknesses observed in Thermal Emission Imaging System (THEMIS) daytime and nighttime infrared data. *Journal of Geophysical Research*, *116*, E10005. <https://doi.org/10.1029/2011je003857>
- Edwards, C. S., & Piqueux, S. (2016). The water content of recurring slope lineae on Mars. *Geophysical Research Letters*, *43*(17), 8912–8919. <https://doi.org/10.1002/2016gl070179>
- Edwards, C. S., Piqueux, S., Hamilton, V. E., Fergason, R. L., Herkenhoff, K. E., Vasavada, A. R., et al. (2018). The thermophysical properties of the Bagnold Dunes, Mars: Ground-truthing orbital data. *Journal of Geophysical Research: Planets*, *123*(5), 1307–1326. <https://doi.org/10.1029/2017je005501>
- Elteto, A., & Toon, O. B. (2010). The effects and characteristics of atmospheric dust during Martian global dust storm 2001A. *Icarus*, *210*(2), 589–611. <https://doi.org/10.1016/j.icarus.2010.07.011>
- Fergason, R. L., Christensen, P. R., Bell, J. F. III, Golombek, M. P., Herkenhoff, K. E., & Kieffer, H. H. (2006). Physical properties of the Mars Exploration Rover landing sites as inferred from Mini-TES-derived thermal inertia. *Journal of Geophysical Research*, *111*, E02S21. <https://doi.org/10.1029/2005JE002583>
- Golombek, M., Grott, M., Kargl, G., Andrade, J., Marshall, J., Warner, N., et al. (2018). Geology and physical properties investigations by the InSight lander. *Space Science Reviews*, *214*(5), 84. <https://doi.org/10.1007/s11214-018-0512-7>
- Golombek, M., Kass, D., Williams, N., Warner, N., Daubar, I., Piqueux, S., et al. (2020). Assessment of InSight landing site predictions. *Journal of Geophysical Research: Planets*, *125*, e2020JE006502. <https://doi.org/10.1029/2020JE006502>
- Golombek, M., Kipp, D., Warner, N., Daubar, I. J., Fergason, R., Kirk, R. L., et al. (2017). Selection of the InSight landing site. *Space Science Reviews*, *211*(1–4), 5–95. <https://doi.org/10.1007/s11214-016-0321-9>
- Golombek, M., Warner, N. H., Grant, J. A., Hauber, E., Ansan, V., Weitz, C. M., et al. (2020). Geology of the InSight landing site on Mars. *Nature Communications*, *11*(1), 1014. <https://doi.org/10.1038/s41467-020-14679-1>
- Golombek, M., Williams, N., Warner, N. H., Parker, T., Williams, M. G., Daubar, I., et al. (2020). Location and setting of the Mars InSight lander, instruments, and landing site. *Earth and Space Science*, *7*(10), e2020EA001248. <https://doi.org/10.1029/2020ea001248>
- Golombek, M. P., Haldemann, A. F. C., Forsberg-Taylor, N. K., DiMaggio, E. N., Schroeder, R. D., Jakosky, B. M., et al. (2003). Rock size-frequency distributions on Mars and implications for Mars Exploration Rover landing safety and operations. *Journal of Geophysical Research*, *108*(E12), 8086. <https://doi.org/10.1029/2002je002035>
- Golombek, M. P., Haldemann, A. F. C., Simpson, R. A., Fergason, R. L., Putzig, N. E., Arvidson, R. E., et al. (2008). Martian surface properties from joint analysis of orbital, Earth-based, and surface observations. In J. Bell (Ed.), *The Martian surface, composition, mineralogy, and physical properties* (pp. 468–497). New York, NY: Cambridge University Press.
- Golombek, M. P., Warner, N. H., Ganti, V., Lamb, M. P., Parker, T. J., Fergason, R. L., & Sullivan, R. (2014). Small crater modification on Meridiani Planum and implications for erosion rates and climate change on Mars. *Journal of Geophysical Research: Planets*, *119*(12), 2522–2547. <https://doi.org/10.1002/2014je004658>
- Grant, J. A., Warner, N. H., Weitz, C. M., Golombek, M. P., Wilson, S. A., Baker, M., et al. (2020). Degradation of homestead hollow at the InSight landing site based on the distribution and properties of local deposits. *Journal of Geophysical Research: Planets*, *125*(4), e2019JE006350. <https://doi.org/10.1029/2019je006350>
- Greeley, R. (1979). Silt-clay aggregates on Mars. *Journal of Geophysical Research*, *84*, 6248–6254. <https://doi.org/10.1029/jb084ib11p06248>
- Grott, M., Spohn, T., Knollenberg, J., Krause, C., Hudson, T. L., Piqueux, S., et al. (2021). *Thermal conductivity of the Martian regolith at the InSight landing site from HP³ active heating experiments*. Earth and Space Science Open Archive. <https://doi.org/10.1002/essoar.10506340.1>
- Grott, M., Spohn, T., Knollenberg, J., Krause, C., Nagihara, S., Morgan, P., et al. (2021). Thermal conductivity of the Martian Regolith at the InSight landing site from HP³ active heating measurements. In *52nd Lunar and planetary science Conference*.
- Hamilton, V. E., Vasavada, A. R., Sebastián, E., de la Torre Juárez, M., Ramos, M., Armiens, C., et al. (2014). Observations and preliminary science results from the first 100 sols of MSL REMS ground temperature sensor measurements at Gale Crater. *Journal of Geophysical Research: Planets*, *119*, 745–770. <https://doi.org/10.1002/2013JE004520>
- Hayne, P. O., Bandfield, J. L., Siegler, M. A., Vasavada, A. R., Ghent, R. R., Williams, J.-P., et al. (2017). Global regolith thermophysical properties of the moon from the diviner lunar radiometer experiment. *Journal of Geophysical Research: Planets*, *122*(12), 2371–2400. <https://doi.org/10.1002/2017JE005387>
- Herkenhoff, K. E., Grotzinger, J., Knoll, A. H., McLennan, S. M., Weitz, C., Yingst, A., et al. (2008). Surface processes recorded by rocks and soils on Meridiani Planum, Mars: Microscopic Imager observations during Opportunity's first three extended missions. *Journal of Geophysical Research*, *113*(E12). <https://doi.org/10.1029/2008je003100>
- Herkenhoff, K. E., Squyres, S. W., Bell III, J. F., Maki, J. N., Arneson, H. M., Bertelsen, P. et al. (2003). Athena microscopic imager investigation. *Journal of Geophysical Research*, *108*(E12), 8065. <https://doi.org/10.1029/2003je002076>

- Hudson, T. L., Deen, R., Marteau, E., Golombek, M., Hurst, K., Spohn, T., et al. (2020). InSight HP³ mole near-surface motion and subsurface implications. In *51st LPSC*.
- InSight_RAD_Science_Team. (2019). *Mars InSight lander radiometer data archive*. <https://doi.org/10.17189/1517568>
- Jakosky, B. M., & Christensen, P. R. (1986). Global duricrust on Mars: Analysis of remote sensing data. *Journal of Geophysical Research*, 91(B3), 3547–3560. <https://doi.org/10.1029/jb091ib03p03547>
- Kieffer, H. H. (2013). Thermal model for analysis of Mars infrared mapping. *Journal of Geophysical Research: Planets*, 118(3), 451–470. <https://doi.org/10.1029/2012je004164>
- Kieffer, H. H., Neugebauer, G., Munch, G., Chase, S. C., & Miner, E. (1972). Infrared thermal mapping experiment: The Viking Mars orbiter. *Icarus*, 16(1), 47–56. [https://doi.org/10.1016/0019-1035\(72\)90136-4](https://doi.org/10.1016/0019-1035(72)90136-4)
- Lorenz, R. D., Lemmon, M. T., Maki, J., Banfield, D., Spiga, A., Charalambous, C., et al. (2020). Scientific observations with the InSight solar arrays: Dust, clouds, and eclipses on Mars. *Earth and Space Science*, 7(5), 12. <https://doi.org/10.1029/2019ea000992>
- Maki, J. N., Golombek, M., Deen, R., Abarca, H., Sorice, C., Goodsall, T., et al. (2018). The color cameras on the InSight lander. *Space Science Reviews*, 214(6), 1–34. <https://doi.org/10.1007/s11214-018-0536-z>
- Marteau, E., Golombek, M., Vrettos, C., & Garvin, J. B. (2021). Soil mechanical properties at the InSight landing site, Mars. In *52nd Lunar and planetary science*.
- Martinez, G. M., Rennó, N., Fischer, E., Borlina, C. S., Hallet, B., Torre Juárez, M., et al. (2014). Surface energy budget and thermal inertia at Gale Crater: Calculations from ground-based measurements. *Journal of Geophysical Research: Planets*, 119(8), 1822–1838. <https://doi.org/10.1002/2014je004618>
- Mellon, M. T., Fergason, R. L., & Putzig, N. E. (2008). The thermal inertia of the surface of Mars. In J. F. Bell (Ed.), *The Martian surface: Composition, mineralogy, and physical properties*. Cambridge University Press.
- Mellon, M. T., Malin, M. C., Arvidson, R. E., Searls, M. L., Sizemore, H. G., Heet, T. L., et al. (2009). The periglacial landscape at the Phoenix landing site. *Journal of Geophysical Research*, 114, E00E06. <https://doi.org/10.1029/2009je003418>
- Mintiti, M. E., Kah, L. C., Yingst, R. A., Edgett, K. S., Anderson, R. C., Beegle, L. W., et al. (2013). MAHLI at the Rocknest sand shadow: Science and science-enabling activities. *Journal of Geophysical Research: Planets*, 118(11), 2338–2360. <https://doi.org/10.1002/2013je004426>
- Moore, H. J., Bickler, D. B., Crisp, J. A., Eisen, H. J., Gensler, J. A., Haldemann, A. F. C., et al. (1999). Soil-like deposits observed by Sojourner, the Pathfinder rover. *Journal of Geophysical Research*, 104(E4), 8729–8746. <https://doi.org/10.1029/1998je900005>
- Morgan, P., Grott, M., Knapmeyer-Endrun, B., Golombek, M., Delage, P., Lognonné, P., et al. (2018). A pre-landing assessment of Regolith properties at the InSight landing site. *Space Science Reviews*, 214(6), 47. <https://doi.org/10.1007/s11214-018-0537-y>
- Morrison, D., Sagan, C., & Pollack, J. B. (1969). Martian temperatures and thermal properties. *Icarus*, 11(1), 36–45. [https://doi.org/10.1016/0019-1035\(69\)90113-4](https://doi.org/10.1016/0019-1035(69)90113-4)
- Mueller, N., Piqueux, S., Lemmon, M. T., Naki, J. N., Lorenz, R. D., Grott, M., et al. (2021). *Near surface properties of Martian regolith derived from InSight HP³-RAD temperature observations during Phobos transits*. Earth and Space Open Archive. <https://doi.org/10.1002/essoar.10506920.1>
- Mueller, N. T., Grott, M., Piqueux, S., Lemmon, M., Maki, J., Lorenz, R., et al. (2020). Mars soil properties from Phobos eclipse observations by InSight HP³ RAD. In *51st Lunar and Planetary Science Conference*.
- Mueller, N. T., Knollenberg, J., Grott, M., Kopp, E., Walter, I., Krause, C., et al. (2020). Calibration of the HP³ radiometer on InSight. *Earth and Space Science*, 7(5), 23. <https://doi.org/10.1029/2020ea001086>
- Mutch, T. A., Arvidson, R. A., Binder, A. B., Guinness, E. A., & Morris, E. C. (1977). The geology of the Viking Lander 2 site. *Journal of Geophysical Research*, 82, 4452–4467. <https://doi.org/10.1029/js082i028p04452>
- Neugebauer, G., Munch, G., Kieffer, H., Chase, J. S. C., & Miner, E. (1971). Mariner 1969 infrared radiometer results: Temperatures and thermal properties of the Martian surface. *The Astronomical Journal*, 76, 719–728. <https://doi.org/10.1086/111189>
- Newman, C. E., & Richardson, M. I. (2015). The impact of surface dust source exhaustion on the Martian dust cycle, dust storms and interannual variability, as simulated by the MarsWRF General Circulation Model. *Icarus*, 257, 47–87. <https://doi.org/10.1016/j.icarus.2015.03.030>
- Nowicki, S. A., & Christensen, P. R. (2007). Rock abundance on Mars from the thermal emission spectrometer. *Journal of Geophysical Research*, 112, E05007. <https://doi.org/10.1029/2006je002798>
- Palluconi, F. D., & Kieffer, H. H. (1981). Thermal inertia mapping of Mars from 60°S to 60°N. *Icarus*, 45, 415–426. [https://doi.org/10.1016/0019-1035\(81\)90044-0](https://doi.org/10.1016/0019-1035(81)90044-0)
- Piqueux, S. (2009). *Heat transfer through particulated media in stagnant gases; model and laboratory measurements: Application to Mars* (pp. 306). Arizona State University.
- Piqueux, S., Buz, J., Edwards, C. S., Bandfield, J. L., Kleinbohl, A., Kass, D. M., et al. (2019). Widespread shallow water ice on Mars at high latitudes and midlatitudes. *Geophysical Research Letters*, 9, 14290–14298. <https://doi.org/10.1029/2019gl083947>
- Piqueux, S., & Christensen, P. R. (2009a). A model of thermal conductivity for planetary soils: 1. Theory for unconsolidated soils. *Journal of Geophysical Research*, 114, E09005. <https://doi.org/10.1029/2008je003308>
- Piqueux, S., & Christensen, P. R. (2009b). A model of thermal conductivity for planetary soils: 2. Theory for cemented soils. *Journal of Geophysical Research*, 114, E09006. <https://doi.org/10.1029/2008je003309>
- Piqueux, S., & Christensen, P. R. (2011). Temperature-dependent thermal inertia of homogeneous Martian regolith. *Journal of Geophysical Research*, 116, E07004. <https://doi.org/10.1029/2011je003805>
- Piqueux, S., & Christensen, P. R. (2012). Visible and thermal infrared observations of the Martian surface during three Phobos shadow transits. *Geophysical Research Letters*, 39, L21203. <https://doi.org/10.1029/2012gl053352>
- Plesa, A. C., Grott, M., Lemmon, M. T., Muller, N., Piqueux, S., Siegler, M. A., et al. (2016). Interannual perturbations of the Martian surface heat flow by atmospheric dust opacity variations. *Journal of Geophysical Research: Planets*, 121(10), 2166–2175. <https://doi.org/10.1002/2016je005127>
- Pohlman, N. A., Severson, B. L., Ottino, J. M., & Lueptow, R. M. (2006). Surface roughness effects in granular matter: Influence on angle of repose and the absence of segregation. *Physical Review E*, 73(3), 9. <https://doi.org/10.1103/PhysRevE.73.031304>
- Presley, M. A., & Christensen, P. R. (1997). Thermal conductivity measurements of particulate materials, Part II: Results. *Journal of Geophysical Research*, 102, 6551–6566. <https://doi.org/10.1029/96je03303>
- Presley, M. A., & Craddock, R. A. (2006). Thermal conductivity measurements of particulate materials: 3. Natural samples and mixtures of particle sizes. *Journal of Geophysical Research*, 111, E09013. <https://doi.org/10.1029/2006je002706>
- Presley, M. A., Craddock, R. A., & Zolotova, N. (2009). The effect of salt crust on the thermal conductivity of one sample of fluvial particulate materials under Martian atmospheric pressures. *Journal of Geophysical Research*, 114, E11007. <https://doi.org/10.1029/2009je003355>

- Putzig, N. E., & Mellon, M. T. (2007a). Apparent thermal inertia and the surface heterogeneity of Mars. *Icarus*, *191*(1), 68–94. <https://doi.org/10.1016/j.icarus.2007.05.013>
- Putzig, N. E., & Mellon, M. T. (2007b). Thermal behavior of horizontally mixed surfaces on Mars. *Icarus*, *191*(1), 52–67. <https://doi.org/10.1016/j.icarus.2007.03.022>
- Sebastian, E., Armiens, C., Gomez-Elvira, J., Zorzano, M. P., Martinez-Frias, J., Esteban, B., & Ramos, M. (2010). The rover environmental monitoring station ground temperature sensor: A pyrometer for measuring ground temperature on Mars. *Sensors*, *10*(10), 9211–9231. <https://doi.org/10.3390/s101009211>
- Shaw, A., Arvidson, R. E., Bonitz, R., Carsten, J., Keller, H. U., Lemmon, M. T., et al. (2009). Phoenix soil physical properties investigation. *Journal of Geophysical Research*, *114*, 19. <https://doi.org/10.1029/2009je003455>
- Smith, M. D., Wolff, M. J., Spanovich, N., Ghosh, A., Banfield, D., Christensen, P. R., et al. (2006). One Martian year of atmospheric observations using MER Mini-TES. *Journal of Geophysical Research*, *111*(E12), E12S13. <https://doi.org/10.1029/2006je002770>
- Spanovich, N., Smith, M. D., Smith, P. H., Wolff, M. J., Christensen, P. R., & Squyres, S. W. (2006). Surface and near-surface atmospheric temperatures for the Mars Exploration Rover landing sites. *Icarus*, *180*, 314–320. <https://doi.org/10.1016/j.icarus.2005.09.014>
- Spiga, A., Banfield, D., Teanby, N. A., Forget, F., Lucas, A., Kenda, B., et al. (2018). Atmospheric science with InSight. *Space Science Reviews*, *214*(7), 64. <https://doi.org/10.1007/s11214-018-0543-0>
- Spiga, A., Murdoch, N., Lorenz, R., Forget, F., Newman, C., Rodriguez, S., et al. (2020). A study of daytime convective vortices and turbulence in the Martian Planetary Boundary Layer based on half-a-year of InSight atmospheric measurements and Large-Eddy Simulations. *Journal of Geophysical Research: Planets*, *126*, e2020JE006511. <https://doi.org/10.1029/2020JE006511>
- Spohn, T., Grott, M., Smrekar, S. E., Knollenberg, J., Hudson, T. L., Krause, C., et al. (2018). The Heat flow and physical properties package (HP³) for the InSight mission. *Space Science Reviews*, *214*(5), 33. <https://doi.org/10.1007/s11214-018-0531-4>
- Stahler, S. C., Widmer-Schmidrig, R., Scholz, J. R., Driel, M., Mittelholz, A., Hurst, K., et al. (2020). Geophysical observations of phobos transits by InSight. *Geophysical Research Letters*, *47*(19), 12. <https://doi.org/10.1029/2020gl089099>
- Statham, I. (1974). The relationship of porosity and angle of repose to mixture proportions in assemblages of different sized materials. *Sedimentology*, *21*, 149–162. <https://doi.org/10.1111/j.1365-3091.1974.tb01786.x>
- Streeter, P. M., Lewis, S. R., Patel, M. R., Holmes, J. A., & Kass, D. M. (2019). Surface warming during the 2018/Mars year 34 global dust storm. *Geophysical Research Letters*, *47*(9), e2019GL083936. <https://doi.org/10.1029/2019GL083936>
- Sullivan, R., Anderson, R., Biesiadecki, J., Bond, T., & Stewart, H. (2011). Cohesions, friction angles, and other physical properties of Martian regolith from Mars Exploration Rover wheel trenches and wheel scuffs. *Journal of Geophysical Research*, *116*, E02006. <https://doi.org/10.1029/2010je003625>
- Sullivan, R., Arvidson, R., Bell, J. F., Gellert, R., Golombek, M., Greeley, R., et al. (2008). Wind-driven particle mobility on Mars: Insights from Mars Exploration Rover observations at “El Dorado” and surroundings at Gusev Crater. *Journal of Geophysical Research*, *113*(E6), E06s07. <https://doi.org/10.1029/2008je003101>
- Sullivan, R., Banfield, D., Bell, J. F., Calvin, W., Fike, D., Golombek, M., et al. (2005). Aeolian processes at the Mars Exploration Rover Meridiani Planum landing site. *Nature*, *436*, 58–61. <https://doi.org/10.1038/nature03641>
- Sweeney, J., Warner, N. H., Ganti, V., Golombek, M. P., Lamb, M. P., Ferguson, R., & Kirk, R. (2018). Degradation of 100-m-scale rocky ejecta craters at the InSight landing site on Mars and implications for surface processes and erosion rates in the Hesperian and Amazonian. *Journal of Geophysical Research: Planets*, *123*(10), 2732–2759. <https://doi.org/10.1029/2018je005618>
- Szwast, M. A., Richardson, M. I., & Vasavada, A. R. (2006). Surface dust redistribution on Mars as observed by the Mars global surveyor and Viking orbiters. *Journal of Geophysical Research*, *111*(E11), E11008. <https://doi.org/10.1029/2005je002485>
- Vasavada, A. R., Piqueux, S., Lewis, K. W., Lemmon, M. T., & Smith, M. D. (2017). Thermophysical properties along Curiosity’s traverse in Gale crater, Mars, derived from the REMS ground temperature sensor. *Icarus*, *284*, 372–386. <https://doi.org/10.1016/j.icarus.2016.11.035>
- Vicente-Retortillo, Á., Martínez, G. M., Renno, N., Newman, C. E., Ordonez-Etxeberria, I., Lemmon, M. T., et al. (2018). Seasonal deposition and lifting of dust on Mars as observed by the curiosity rover. *Nature Scientific Reports*, *8*, 17576. <https://doi.org/10.1038/s41598-018-35946-8>
- Viudez-Moreiras, D., Newman, C. E., Forget, F., Lemmon, M., Banfield, D., Spiga, A., et al. (2020). Effects of a large dust storm in the near-surface atmosphere as measured by InSight in Elysium Planitia, Mars. Comparison with contemporaneous measurements by Mars science laboratory. *Journal of Geophysical Research: Planets*, *125*(9), 24. <https://doi.org/10.1029/2020je006493>
- Vu, T. H., Piqueux, S., Choukroun, M., Edwards, C. S., Christensen, P. R., & Glotch, T. D. (2019). Low-temperature specific heat capacity measurements and application to Mars thermal modeling. *Icarus*, *321*, 824–840. <https://doi.org/10.1016/j.icarus.2018.10.004>
- Walker, R. (1964). *Infrared photometry of stars and planets* (pp. 190). Harvard University.
- Wang, A., Haskin, L. A., Squyres, S. W., Jolliff, B. L., Crumpler, L., Gellert, R., et al. (2006). Sulfate deposition in subsurface regolith in Gusev crater, Mars. *Journal of Geophysical Research*, *111*(E2), E02S17. <https://doi.org/10.1029/2005je002513>
- Warner, N. H., Golombek, M. P., Sweeney, J., Ferguson, R., Kirk, R., & Schwartz, C. (2017). Near Surface stratigraphy and Regolith production in southwestern Elysium Planitia, Mars: Implications for Hesperian-Amazonian terrains and the InSight lander mission. *Space Science Reviews*, *211*(1–4), 147–190. <https://doi.org/10.1007/s11214-017-0352-x>
- Warner, N. H., Grant, J. A., Wilson, S. A., Golombek, M. P., DeMott, A., Charalambous, C., et al. (2020). An impact crater origin for the InSight landing site at Homestead Hollow, Mars: Implications for near surface stratigraphy, surface processes, and erosion rates. *Journal of Geophysical Research: Planets*, *125*(4), 36. <https://doi.org/10.1029/2019je006333>
- Weitz, C. M., Anderson, R. C., Bell, J. F., Farrand, W. H., Herkenhoff, K. E., Johnson, J. R., et al. (2006). Soil grain analyses at Meridiani Planum, Mars. *Journal of Geophysical Research*, *111*(E12), E12S04. <https://doi.org/10.1029/2005je002541>
- Weitz, C. M., Grant, J. A., Golombek, M. P., Warner, N. H., Hauber, E., Ansan, V., et al. (2020). Comparison of InSight Homestead Hollow to Hollows at the Spirit Landing Site. *Journal of Geophysical Research: Planets*, *125*(7), 17. <https://doi.org/10.1029/2020je006435>
- Weitz, C. M., Sullivan, R. J., Lapotre, M. G. A., Rowland, S. K., Grant, J. A., Baker, M., & Yingst, R. A. (2018). Sand grain sizes and shapes in Eolian bedforms at Gale Crater, Mars. *Geophysical Research Letters*, *45*(18), 9471–9479. <https://doi.org/10.1029/2018gl078972>
- Wilson, R. J., & Guzewich, S. D. (2014). Influence of water ice clouds on nighttime tropical temperature structure as seen by the Mars Climate Sounder. *Geophysical Research Letters*, *41*(10), 3375–3381. <https://doi.org/10.1002/2014gl060086>
- Wilson, R. J., Lewis, S. R., Montabone, L., & Smith, M. D. (2008). Influence of water ice clouds on Martian tropical atmospheric temperatures. *Geophysical Research Letters*, *35*(7), L07202. <https://doi.org/10.1029/2007gl032405>
- Zent, A. P., Hecht, M. H., Cobos, D. R., Wood, S. E., Hudson, T. L., Milkovich, S. M., et al. (2010). Initial results from the thermal and electrical conductivity probe (TECP) on Phoenix. *Journal of Geophysical Research*, *115*, 23. <https://doi.org/10.1029/2009je003420>
- Zuber, M. T., Smith, D. E., Solomon, S. C., Muhleman, D. O., Head, J. W., Garvin, J. B., et al. (1992). The Mars observer laser altimeter investigation. *Journal of Geophysical Research*, *97*(E5), 7781–7797. <https://doi.org/10.1029/92je00341>